January 2018

Digital Rock Reconstruction And Property Calculation Of Fractured Shale Rock Samples

Hongsheng Wang

DIGITAL ROCK RECONSTRUCTION AND PROPERTY CALCULATION OF FRACTURED SHALE ROCK SAMPLES

by

Hongsheng Wang

Bachelor of Science, China University of Petroleum (East China), 2013

Master of Science, China University of Petroleum (East China), 2016

A Thesis

Submitted to the Graduate Faculty

of the

University of North Dakota

for the degree of

Master of Science

Grand Forks, North Dakota

December

2018

This thesis, submitted by Hongsheng Wang in partial fulfillment of the requirements for the Degree of Master of Science from the University of North Dakota, has been read by the Faculty Advisory Committee under whom the work has been done and is hereby approved.

Minou Rabiei 11/29/18
Minou Rabiei, Chairperson Date

Kegang Ling 11/29/2018
Kegang Ling, Committee Member Date

Hui Pu 11/29/2018
Hui Pu, Committee Member Date

This thesis (or dissertation) is being submitted by the appointed advisory committee as having met all of the requirements of the School of Graduate Studies at the University of North Dakota and is hereby approved.

Dean of the School of Graduate Studies

December 5, 2018
Date

Title Digital Rock Reconstruction and Property Calculation of Fractured Shale Rock Samples

Department Petroleum Engineering

Degree Master of Science

In presenting this thesis in partial fulfillment of the requirements for a graduate degree from the University of North Dakota, I agree that the library of this University shall make it freely available for inspection. I further agree that permission for extensive copying for scholarly purposes may be granted by the professor who supervised my thesis work or, in his absence, by the Chairperson of the department or the dean of the Graduate School. It is understood that any copying or publication or other use of this thesis or part thereof for financial gain shall not be allowed without my written permission. It is also understood that due recognition shall be given to me and to the University of North Dakota in any scholarly use which may be made of any material in my thesis.

Hongsheng Wang

November 29, 2018

TABLE OF CONTENTS

LIST OF FIGURES

LIST OF TABLES

ACKNOWLEDGEMENTS

I would like to thank my committee members, Dr. Minou Rabiei (Chairperson), Dr. Kegang Ling and Dr. Hui Pu, for their valuable advices on my research and critical reviews on my graduation thesis. Also, I appreciate the education and research experience provided by the Petroleum Engineering Department and the Energy & Environmental Research Center, the University of North Dakota.

Thank everyone who offered their selfless help, while I completed my research about the digital rock and fracture quantification.

ABSTRACT

As the preferential flow channels in the shale reservoir, the fracture systems including the natural micro-cracks and hydraulic fractures have received great attention from the whole energy industry worldwide. However, it is challenging to quantify the fracture systems in the shale rocks precisely because most of well-developed "histogram-based" image processing techniques cannot handle the case of small target segmentation. Because the fracture apertures are very thin, the over-segmentation or insufficient segmentation would lead to significant error in the quantification, including the fracture porosity, aperture, length, tortuosity etc., which would lead to serious mistakes to the property calculation.

In this research, two novel image processing methods are proposed. The self-adaptive image enhancement method employs incomplete beta function and simulated annealing algorithm to modify the grayscale intensity histogram. The contrast between the target and the background of the transformed gray image reaches the maximum. Also, "self-adaptive" means the enhancement process is specified by the input images. The comparison of segmentation results before and after the image enhancement show that the target becomes more obvious to the naked eyes and the precise fracture porosity of the test image is 4.02 %.

The multi-stage image segmentation (MSS) method combines the global and local information of the image to finish the segmentation. The generated three-dimensional model provides visualization of the fracture systems existing in the core. Also, the important parameters of the fractures can be obtained, including aperture, length, tortuosity, and porosity. Compared with the

real permeability from the core-flooding experiments, the permeability calculated from the MSS method has the minimum error of 22.1 %. The results show that the proposed methods in this research can be effective tools for the precise quantification of the thin fracture systems.

CHAPTER I

INTRODUCTION

With the depletion of conventional energy resources, the unconventional resources will become more and more important around the world as new sources of energy (Hoffman & Shoaib, 2014; Jia et al., 2019; Lee, 2008). During the last two decades, with the rapid development of advances in horizontal drilling and hydraulic fracturing, unconventional oil reservoir (Miller et al., 2008), including the Bakken Formation in North Dakota and Montana, the Eagle Ford in Texas, and the Niobrara in Colorado and Wyoming, have become the leading oil production areas in North America. Although there are some differences among these reservoirs, the common aspect is that they have extremely low porosity and low permeability (Todd & Evans, 2016). Therefore, the primary recovery factor remains very low, about 5 - 10 % (Jia et al, 2018).

Although Bakken formation is a famous as shale reservoir, it has a dolomitic siltstone lithology originally. The Bakken formation includes three main members (Flannery & Kraus, 2006): (1) Upper Bakken formation – Organic-rich black pyritic shale, (2) Middle Bakken formation – Fine-grained sandstone or middle silty dolostone ,about 15 ft thick, and (3) Lower Bakken formation – Organic-rich black pyritic shale. The total organic content of the upper shale has been measured up to 40 % (Kumar & Hoffman, 2013). Due to the absence of an adjacent high-permeability formation, internal fluid pressures rose during the conversion of kerogen to oil and created natural fractures in the shale. Also, the treatment of multi-stage fracturing create a better reservoir connection and inner link of the natural or existing facture systems (Miller et al., 2008; Jia et al,

2018).

Not like the conventional large-scale reservoirs that have been characterized through many methodologies, shale formation has not yet undergone advanced characterization, and much remains to be done (Tahmasebi et al, 2015). The fracture systems in the shale reservoir, including the natural micro-cracks and the visible hydraulic fractures, serve as the preferential flow conduits and always dominate the mass transfer in geological materials. The most commonly precise fracture quantification techniques are the imaging logging (Lai et al, 2017) and core data analysis (Jia et al, 2017). However, these techniques have obvious drawbacks: First, the current methods ignore the inherent micro-cracks, which will lead to the conductivity ability of the geological model is much lower than the real reservoir condition (Dewhurst & Siggins, 2006). For most of the fracture modellings, the engineers use the implicit fracture modelling to offset the absence of the natural micro-cracks, which is entirely based on the statistical properties set by the users to match the historical data, not the real geological information (Xu & Dowd, 2010). Also, the core data analysis in the lab is time-consuming and expensive, which will cost days or even weeks to operate the lab experiments (Jia et al, 2018). Besides, some experiments will destroy the original structure of the cores, which means these experiments are one-time events. All these factors determine that some core data analysis experiments have very poor repeatability.

Considering the problems about current fracture quantification techniques, the researchers proposed effective novel visualization solutions using digital rock theory, which are non-destructive to the cores. The high-resolution scanning technique provides high-quality two-dimensional images, which show the structure of micro-cracks and three-dimensional models consisting of rock matrix and fracture system. With the obvious advantages of digital rock

technologies, the researchers have finished some micro-level studies in the field of petroleum engineering, geochemistry, geophysics etc.

1.1 Literature Review

A substantial experimental data is a cornerstone of most geophysical interpretation and reservoir simulation, because any transformation from remotely measured quantities, such as EM-derived resistivity or seismic impedance, to the reservoir properties, including permeability, porosity, saturation, should be either an experimental regression or a theoretical model, which is calibrated and verified by experimental data (Dvorkin et al., 2008).

Compared with the traditional lab experiments using real rock samples (cores, pluggings, and cuttings), the digital rock simulation experiments have some obvious advantages including:

(1) Lower cost:

Avoiding the problemic process of sample coring, transportation, and pre-processing phase and expensive real experimental apparatus, digital rock theory can save money and time for the researchers.

(2) More feasible and applicable:

The simulation using the digital rock can be repeated in acceptable time span for many times and the experimental conditions can be set by the users, which means some complicated experimental conditions can be achieved.

(3) Better Micro-level Description:

Most of the lab experiments are established based on the Darcy's law, which can't be used for micro-level study. Digital rock makes the micro-level characterization possible, which provides a novel prospective to study the micro-seepage-theory.

Because of these advantages, the digital rock theory, as a novel perspective to observe the inner structure of the rock sample and obtain the experimental data, has been studied, developed, and applied to different research fields. The key procedure of digital rock is the three-dimensional model reconstruction. For different research sample, different reconstruction methods were proposed and test. Also, the concerning application of digital rock theory in this research is the fracture quantification techniques.

1.1.1 Digital Rock Theory

Digital rock is the concept of discretization of the real rock sample, including rock matrix and pores, into numerous pixels, whose length is determined by the resolution of scanning image. Using digital rock with high resolution, researchers can observe the inner structure of the microporous media precisely, which builds the foundation of high-accuracy simulation of fluid flow, distribution, and storage (Andrä et al., 2013).

The computational methods used to simulate the fluid flow in the digital rock are very sensitive to the size of the digital rock or how many pixels contained in the model. The simulation time will increase drastically with the increase of the size of the digital rock. The huge computation brought by high-resolution pixels has been restricting the development of digital rock technology. There are two effective ways to solve this problem: (1) Develop an advanced computer with stronger computational ability, (2) Develop a simplified model based on the digital rock – the pore network model (Zhang, 2015). A good pore network model can be used to study the distribution and conductivity of fluids in the rock sample precisely, and more importantly, save the computing time greatly. Taking the pore network model as a study object, the researchers have solved some micro-

level problems, including the seepage law and distribution of water and oil phases in water flooding, the change of oil properties caused by surfactant in chemical flooding etc.

In different research fields, including petroleum engineering, geophysics, geochemistry etc., digital rock modelling has been applied widely. For reservoir description and modelling, the characterization of the complex pore network in the rock sample is the most direct application of digital rock, from nanometer to centimeter, then to understand and predict rock properties at the sub-plug scale (Blunt et al., 2002; Bakker & Øren, 1997). As a novel core analysis method at sub-plug scale, digital rock has been proven to provide significant commercial values (Lopez et al., 2010).

Geometrical, petrophysical, and multi-phase flow properties depend strongly on the scale of the research target. However, the traditional characterization methods of rock samples are limited to mm-scale (Wu et al., 2007; Wu et al., 2008). It is necessary to characterize the rock heterogeneity of different rock types at micro-scale or even nano-scale, which can help to recognize which rock type has more important effects on fluid flow properties, especially for multi-phase flows. For multi-phase flow, it is important to understand how heterogeneities interact with fluid forces, including gravity, capillary, and viscous, acting on different scales (Kalam et al., 2012). Lopez et al. (2012) applied the multi-scale imaging and modelling method to characterize heterogeneity and predicted the petrophysical properties at different scales for more than 100 core samples. In that work, multi-scale X-ray computed micro-tomography imaging and three-dimensional rock modelling succeeded characterizing the heterogeneity, dominant pore size, and rock types, from micritic facies (nm-scale), intergranular porosity (μm-scale), vuggy porosity (mm-scale) to whole rock core (cm-scale). Then, some petrophysical properties, including porosity,

permeability, m-exponent, n-exponent, and primary drainage were calculated and compared with available core analysis data of same rock samples, which did match the calculation results very well.

The capillary pressure relationships are the most important parameters, which can be used to provide supplementary data for relative permeability estimates; estimation of fluid contacts, transition zones, and reservoir initial fluid saturations; evaluation of sealing pressure and displacement pressure. There are three traditional methods to determine capillary pressure curves: the centrifuge method (CM) (Hassler & Brunner, 1945), the porous plate (PP) (Leverett, 1941), and the mercury intrusion porosimetry (MICP) (Purcell, 1949). In general, the multi-speed centrifuge method (CM) is the most common choice for routine core analysis, because of the comprehensive consideration of speed and accuracy. However, how to set the rotational speed schedule is a long-standing problem. Shikhov and Arns (1997) use the digital rock to assist in the estimation of experimental equilibrium times and act as a useful tool in speed schedule design.

Permeability is another important parameter to predict the oil and gas production in the reservoir, contaminants migration in aquifers and soils, etc. The traditional method, which is the direct measurement of permeability in the lab, is accurate, but time-consuming and expensive. Also, the preparation of rock sample limits the application of the direct approaches. In recent years, the Kozeny-Carman relation (Dullien, 2012), based on the simple cylindrical pore geometry, has been applied widely. The advantage of Kozeny-Carman relation is the easy use. Mavko and Nur (2004) used the Kozeny-Carman relation to predict the permeability from the 2D thin image, and the results matched the lab experiments very well. However, the disadvantages of this method are also very obvious. The models used in the Kozeny-Carman relation are empirical, which means

the models give little insight into the relationship between permeability and pore geometry. Also, some parameters, including the formation factors and the specific surface area, should be calibrated with experimental data. As a result, the Kozeny-Carman correlation can not be applied to the porous media with complex pore system. Blair et al. (1993) improved the models, and the results are highly sensitive to the resolution of thin section images. In recent years, with the development of the three-dimensional scanning techniques, the applications of the Lattice-Boltzmann (L-B) method to predict permeability yielded excellent results. Keehm et al. (2004) reconstructed the 3D model using sequential indicator simulation and simulated the permeability. The results showed that the Lattice-Boltzmann method can handle the porous media with complex pore network very well.

1.1.2 Three-dimensional Model Reconstruction

The key point of digital rock is the three-dimensional model construction. Based on the different methods proposed by the researchers, the three-dimensional model reconstruction techniques can be divided into 2 categories: Direct method and indirect way.

Experimental Physical Method – Direct Method

There are many tools available to image rocks with different resolutions. Among them, computerized tomography (CT) and other X-ray scanning technologies are popularly used to create three-dimensional rock images that show the internal pore structures, their connectivity and mineral compositions.

There some common types of scanning techniques, including the followings:

- Conventional CT (millimeter resolution)
- Micro-CT (between 1 and 5 μm resolution)

- Laser Scanning Fluorescence Microscopy (submicron, approximately 250 nm resolution)
- Transmission Electron Microscopy (TEM) (approximately 100 nm resolution)
- Scanning Electron Microscope (SEM) (approximately 5 nm resolution)
- Atomic Force Microscopy (AFM) (approximately 10 nm resolution)
- Focused Ion Beam-Scanning Electron Microscope (FIB-SEM, three-dimensional images, between 1 and 5 nm resolution)

Based on the imaging results, the scanning techniques are briefly reviewed below:

(1) Focused Ion Beam–Scanning Electron Microscope (FIB-SEM)

FIB-SEM is a new 3D scanning technique, which is based on the serial-section imaging method and uses the focused-ion-beam (FIB) technology. First of all, generate the 2D image of the surface of the rock sample. Then, accelerated gallium (Ga+) will be used to sputter the atoms from the sample surface, and a 2D image of the new surface will be generated. Repeat this process until the whole rock sample is scanned. At last, all the 2D images will be stacked in serial sequence to reconstruct the 3D model. The milling layer can be as thin as 10 nm (Tomutsa et al., 2007).

The application of FIB-SEM is very extensive. First of all, FIB is the most common method to mill the rock sample. Also, in the field of earth science, Vogel and Roth (2001) used pore-network generated by FIB-SEM to study the pore geometry and transport processed (Pore-size distribution and connectivity function) in soil. In the field of microelectronics, to verify the design, analyze failure, and modify the circuit, Orloff et al. (2004) used FIB-SEM to access individual components with nanoscale accuracy. In the field of material science, the sectional images generated by FIB-SEM used by Kubis et al. (2004) to analyze the alloy components. In the field of petroleum engineering, the major application of FIB-SEM is to analyze the micro-pore structure.

Lymberopoulos and Payatakes (1992) obtained the topological, geometrical, and pore-size correlation properties of porous materials. Tomutsa et al. (2007; 2003; 2004) solved the fluid flow in the tight gas sands, diatomite and chalk using FIB-SEM to obtain pore structure with a submicron-scale resolution.

The advantage of FIB-SEM is its high resolution and the three-dimensional result. However, it carries some shortcomings. Because the processes of milling and polishing rock sample take a very long time, and it destroys the structure of the rock sample, it is not very practical.

(2) Computed Tomography Scanning

In the early 1980s, Elliott et al. (1995) invented the first computed tomography machine. Then CT was widely used in the field of medicine. Coming to the 21st century, Dunsmuir et al. (1991) discovered the potential of CT scanning to characterize the inner structure of porous media. With the development of CT scanning techniques, its applications in the field of petroleum engineering and geo-material has become very common now. There are some kinds of CT machines used in the field of petroleum engineering: conventional CT, micro-CT and synchronic powered transmission CT (Dong, 2007; Zhang, 2015).

The resolution of images generated by the synchronic CT is much higher than the conventional CT. As a result, conventional CT is used to characterize the weakly cemented porous media, such as loose carbonate, and the synchronic CT can be used to generate the 3D model of tight media, such as shale rock [44]. However, the expense of synchronic CT scanning is very high and the processing time is too long, which lead to the limited applications of synchronic CT.

(3) Laser Scanning Confocal Microscopy Scanning

FIB-SEM and CT scanning are commonlu used to generate the 3D model of the rock sample. Another method to generate the 3D model was introduced by Fredrich et al. (1992). In this method, first, inject an epoxy doped with a fluorochrome with fluorescent wavelength matching the excitation wavelength. Then, use the laser scanning confocal microscopy to generate the three-dimensional pore structure of geological materials. The advantage of this method is the high-resolution of the image, however, restricted to the pre-process – injection of epoxy, it can only be applied to the thin rock slice modelling, whose size is very small. Also, for the tight rock samples, such as tight carbonates or shale rocks, it is difficult to determine whether the saturation process is finished or not, and the saturation process is very time-consuming.

(4) Scanning Electron Microscope

SEM is an effective scanning technique to generate 2D images with high resolution, which can be 5 nm. The scale of SEM output images is perfect for the tight rock sample, like shale rock. It can show both the large and small round pores in mature kerogen (darker area) of the rock samples (Curtis et al., 2010), which exist in the Upper and Lower Bakken formation. Fig. 1-1 is the example of SEM image for a tight shale rock sample. The size of the sample is 2 μm and the resolution is about 2.9 nm. The pores and the kerogen inside can be observed clearly.

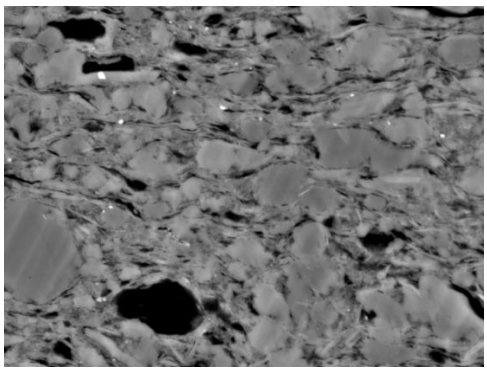

Fig. 1-1 Example of SEM Output Image

Numerical Reconstruction Method – Indirect Method

Numerical reconstruction method is based on the scanning images, using some different statistical methods or rock formation simulation to reconstruct the digital rock. Until now, the traditional reconstruction methods include Gaussian Simulation Method, Simulated Annealing Method, Process-based Simulation Method, and Markov Random Reconstruction Method.

First proposed by Joshi (1974), Gaussian simulation method is based on the statistical parameters from the image analysis of rock slice and generate a dataset, composed of the individual Gaussian variables. Then, operate a linear transformation to the dataset, which can make the individual variables under the constraints of porosity and two-point correlation function. The last step is to transform the Gaussian field to digital rock by the nonlinear transformation. Quiblier (1984) extended the model from two-dimension to three-dimension. Adler et al. (1990) improved previous models by incorporating the periodic boundary conditions, establishing the three-dimensional pore network of Fontainebleau sandstone sample. Some later researchers ameliorated the algorithms. Ioannidis et al. (1999) introduced Fourier transformation to make the speed faster. Hilfer (1991) introduced porosity distribution and seepage probability distribution function to describe the characterization of pore space. Torquato & Lu (1993) and Levitz (1998) used chord-length distribution function to improve the model. However, the connectivity of the reconstructed model was poor.

To make the reconstructed model more similar to the real rock sample, especially the pore connectivity, Hazlett (1997) proposed a simulated annealing method to consider more information about rock properties. The target function (System energy) of simulated annealing is the sum-of-squared-difference between statistical properties of reconstruction and real sample. By updating

the system, when the system energy reaches the minimum, the digital rock is obtained. The results show that the reconstruction can reflect the properties involved in the modelling effectively. Hidjat et al. (2001) combined Gaussian simulation method and simulated annealing by using the result of the Gaussian simulation method as the input of the simulated annealing method, which made the speed faster.

Unlike the modelling methods above, Bryant & Blunt (1992) proposed the idea that the simulation process should follow the process of the rock formation (sedimentation, compaction, and diagenesis) because the pore distribution is not random, but related. The new model can predict the pore connectivity precisely. Later, Bakke and Øren (1997) improved this method by considering the influence of the particle size and they also involved the properties of rock from the analysis of rock slice. The reconstruction can reflect the geometric property and connectivity very well.

Later, some researchers applied improvement on process-based simulation methods. More particle shapes were considered, including sphere, eliptic and non-sphere were considered. The type of clay as the filling material was not limited to feldspar, but also chlorite and illite were also considered. Pilotti (2000) and Coelho et al. (1997) proved that by these improvements, the output model could reflect the heterogeneity and connectivity of the real rock sample. However, for the rock with complex pore network, the process of the rock formation is too difficult to simulate.

Okabe & Blunt (2005) proposed another novel method – Multi-point statistical method. This method uses the geostatistical techniques of pixel-based representations to reproduce large-scale patterns. The two-dimensional thin images can provide multi-point statistics, describing the statistical relation between multiple spatial locations, to generate the three-dimensional pore space

reconstruction. Wu et al. (2004) based on the Markov random filter statistical model, uses two-points and five-point local templates to obtain the characterization of the interface between the rock matrix and pore and involve the characterization in the model. The three-dimensional model from this method has a pore system with excellent connectivity and fast modelling speed.

Compared with other reconstruction methods, the multi-point statistical method and Markov random reconstruction method can model any rock types or any diagenetic process. However, the modelling is based on the assumption that the rock is isotropic, which is the biggest disadvantage of these two methods.

According to the features of different reconstruction methods, researchers applied the three-dimensional reconstruction techniques to different study target in different research fields. Ni et al. (2017) studied pore-fracture system in the coal reservoir to simulate gas migration. Because the traditional methods to obtain the structural characteristics in coal, such as low-temperature liquid nitrogen adsorption, carbon dioxide adsorption, and mercury intrusion method, are relatively poor in describing the connectivity of pore and fracture, it will lead into large error in predicting the permeability (Hao, 1987; Xue et al., 2012). For coal reservoir, FIB-SEM could damage the coal sample easily during peeling, the scope of observation from nano-CT is too small, and micro-CT can not reflect detailed information about the pore-fracture system. The authors used different scanning electron microscopes and optical microscope to get images of different scales and extract microscopic fracture information in different scales of pore-fracture network using image processing. The three-dimensional model was reconstructed using Monte Carlo methods. Finally, the authors predicted the permeability precisely and studied the contribution of the pore-fracture network to permeability.

Karimpouli and Tahmasebi (2016) proposed a novel reconstruction method – Cross-correlation based simulation (CCSIM). The main idea of this method is to use a crosscorrelation function along a one-dimensional raster path and to combine it with efficient strategies to honor the continuity and pattern reproducibility to generate realizations of the porous medium that match the image (Tahmasebi et al., 2012; Tahmasebi et al., 2015). This work provided a novel idea to study high heterogeneity and variability. Implementing the laboratory approach, which measures a significant number of samples, the authors studied the trends by subsampling of a large digital samples. Operate cross-correlation based simulation to reconstruct the three-dimensional model of subsamples, and the subsequent steps remain as standard digital rock physics, including segmentation and rock physical property calculation. Verified by the results of the laboratory measurements and the standard digital rock physics, they obtained results which described the rock heterogeneity very well.

Yeong and Torquato (1998) applied the simulated annealing method to reconstruct the structure of general random heterogeneous media from limited morphological information. They reconstructed some one-dimensional and two-dimensional model microstructures and the real sandstone image using morphological information, which contained in the lineal-path function, two-point correlation function or both of them. Also, the authors extended the procedure form two-dimensional slices to reconstruct three-dimensional isotropic structure, and more complex media, like anisotropic structures and comparison between the reference system and reconstructed systems, showing good match of the results. Manwart et al. (2000) employed the simulated annealing algorithm to generate a stochastic model for a Fontainebleau and a Berea sandstone, with the pre-set lineal-path function, two-point probability function, and pore size distribution

function. The authors found that when the temperature of annealing decreases quickly enough, the isotropic and percolating configuration can be yielded. The results showed that the match between the original sandstones and the reconstructions was very good. Also, the mean survival time of a random walker in the pore space was reproduced with good accuracy.

1.1.3 Fracture Quantification

After the generation of the high-resolution reconstructed grayscale images, the next step is its application. For this research, the application of digital rock in the fracture quantification is the most concerning problem, which can be used for property calculation, rock characterization, and reservoir simulation.

Iacoviello et al. (2017) used micro- and nano- X-ray CT imaging techniques to study organic-rich, finely laminated mudstones as the source and reservoir of unconventional gas. A big problem in the gas production in shale reservoir is that the productivity decreases sharply in gas recovery or low rates of gas production in the 4 to 6 years after the fracturing, which means there are large volumes of gas left in the reservoir. The declined curve is the signal of bad interconnectivity in the pore and fracture system, which caused by the inefficient stimulation measurements. Pores existing at mineral boundaries and with organic matter are very small, whose size is between a few microns and hundreds of nanometers. Micro- and nano-CT scanning provide a valuable tool to study the three-dimensional distribution and connectivity network of the pore and fracture system, which act as the routes for the trapped gas from the reservoir to the borehole.

Lai et al. (2017) studied fracture analysis of tight gas sandstone – the Lower Cretaceous Bashijiqike sandstone, using industrial computed tomography. The high-resolution industrial X-ray CT provided a three-dimensional quantitative characterization of the fracture geometries.

Using the two-dimensional slice analysis, the authors obtained the corresponding fracture area, length, aperture, fracture porosity, and fracture density. Then, they created the three-dimensional image using the volume-rendering software. In the three-dimensional model, they colored the vug (open fracture) in cyan and calcite-filled fractures in magenta. By three-dimensional counting, the surface area, volume, porosity, and aperture can be calculated or estimated. Finally, they determined the connectivity of fractures is by comparing fracture parameters with permeability.

The key technique of fracture quantification is image segmentation, where the pixels are classified into void space and mineral phases. Segmentation techniques for images of porous media were established and generated (Wildenschild et al., 2002; Wildenschild et al., 2013).

The most common image segmentation techniques are histogram thresholding algorithms, which rely on the identification of a single grayscale value to partition intensities into different categories. Ketcham et al. (2010) used X-ray CT to image fractures in the solid samples. In their research, they proposed an improved method for fracture segmentation – the Inverse Point-spread Function (IPSF). The results showed that on CT scans of homogeneous natural samples show that IPSF methods provide more precise results than others. Porter and Wildenschild (2010) hired the image analysis algorithms, including voxel counting, two-point correlation functions, and the porous media marching cubes to study the identification of phases and estimation of porosity, saturation, solid surface area, and interfacial area between fluid phases from grayscale X-ray microtomographic image data. Elliot and Heck (2007) used a histogram thresholding method – Low variance voxel segmentation techniques, to study that three-dimensional consideration should be used in the analysis of CT and intact soil columns.

Another group of segmentation algorithms, including edge detection and region-grow, used spatial information about local variation in grayscale intensity (Nikolaidis & Pitas, 2000). Noiriel et al. (2013) studied the effects of reactive transport on fracture geometry and fluid flow through an integrated experimental and modelling approach. They used the synchrotron X-ray micro-tomography experiments to obtain the images of fracture geometry under different conditions. Also, the edge detection was used to extract the aperture and fracture walls from three-dimensional images. The experimental measurements, including fluid chemistry, hydraulic tests, and computation of Navier-Stokes flow verified the accuracy of the algorithm. More sophisticated methods have also been developed, by using additional criteria or by combining more than one basic segmentation scheme, such as active contour method (Yushkevich et al., 2005; Frangi et al., 1998).

1.2 Research Statement

After overview of the scanning techniques, we chose high-resolution SEM to generate the two-dimensional images of the natural micro-cracks in the shale slices because its resolution can be nano-scale. Also, we chose X-ray CT scanning to generate the three-dimensional image of the hydraulic fracture systems because it is indispensable for non-destructive observation of the geometry of fractures and its resolution can be micro-scale. In this research, we proposed two novel image processing methods – self-adaptvie image enhancement method and multi-stage image segmentation method. The self-adaptive image enhancement can modify the grayscale intensity histogram of the two-dimensional SEM scanning images by using incomplete beta function as transformed operator. The optimization process of the parameters in incomplete beta function is finished using simulated annealing and only determined by the input data, that is why

this method is “self-adaptive”. The multi-stage image segmentation method can combine the global information and local information of the whole image, which employs the entropy function and indicator kriging to classify the boundary pixels.

1.2.1 Research Significance

For the result images generated by various high-resolution scanning techniques, the fracture systems is the small target compared with the background. The image segmentation of small target has been a challenging topic. Although over the past decades, the application of advanced scanning techniques to the three-dimensional visulization and quantification of the rock sample has received great success, most of the well-developed methods are mainly used for the carbonate reservoir, where the pores and the fracture systems are obvious when compared with the background. Most of image processing techniques are based on the Otsu’s method (Otsu, 1979; Christe et al, 2011; Baker et al, 2012), which are “histogram-based” image segmentation techniques using the global threshold value. The information of the small target cannot be reflected in the grayscale intensity histogram because the contrast between the target and the background is not strong enough. The application of “histogram-based” image segmentation techniques would lead to insufficient segmentation results. Also, the uneven illumination on the whole image would cause the problem of partial over-segmentation or partial insufficient segmentation because only the global information is considered. Because the fracture apertures are commonly very small, any over-segmentations and insufficient segmentations would cause big error in property calculation. To quantify the thin fracture systems in the shale rock precisely, novel image processing methods that can enhance the small target and employ the global and local information of the images are needed.

1.2.2 Research Objectives

In this research, two novel image processing methods are proposed, whose goal is to make the fracture quantification more precise. For the self-adaptvie image enhancement method, the research target would be the high-resolution SEM scanning images with natural micro-cracks, whose grayscale intensity histograms are highly concentrated distributed. This method is expected to optimize the parameters used in the trasformed operator for each specific input image, to make the contrast between the small target and the background the maximum. After the image enhancement, the fracture systems should be more obvious to the naked eyes and the distribution of the corresponding grayscale intensity histogram should be wider to include more information into the following image segmentation. For multi-stage image segmentation method, the research target would be the X-ray CT images with thin hydraulic fractures. This method is expected to combine the global and local information to segment the fractures, which is the improvement especially for the boundary pixel calssification. The segmentation results should match the core-flooding data in an acceptable error with acceptable running time, which means the quantification is precise.

CHAPTER II

METHODOLOGY

From the review of previous work on image processing, the self-adaptive image enhancement method and multi-stage image segmentation method are proposed in this research. This chapter describes the detailed theories and methods related to these novel image processing methods and the experimental equipments and samples: Section 2.1 – scanning electron microscope and image enhancement method, Section 2.2 – X-ray Computed Tomography and multi-stage image segmentation method, Section 2.3 – Kozeny-Carman relation for permeability calculation, and Section 2.4 – Data acquisition and pre-processing.

2.1 Scanning Electron Microscope and Image Enhancement Method

This section focuses on the high-resolution SEM scanning technique and two-dimensional image processing, mainly on image enhancement. To quantify the natural micro-cracks in the shale rock slices from Bakken Formation, the contrast between the image background – rock matrix, and the target – micro-cracks should be enhanced. In this section, the basic knowledge of SEM scanning is introduced, which is section 2.1.1. Section 2.1.2 explains the theories related to the self-adaptive image enhancement technique, including Otsu's method, incomplete beta function and simulated annealing algorithm.

2.1.1 Introduction to Scanning Electron Microscope

The scanning electron microscope (SEM) is the type of electron microscope. Using a focused beam of electrons to scan the surface, the SEM produces images of the sample surface. The electrons interact with the atoms on the sample surface, generating different signals which contain information on the topography and composition of the sample surface. The electron beam is scanned in a raster scan pattern. The combination of the detected signals and the beam's position produces an image. SEM can achieve 1-nanometer resolution. For conventional SEM, the specimens can be observed in a high vacuum, and for variable pressure or environmental SEM, specimens can be observed in low vacuum or wet conditions. With some specialized instruments, the condition can be at a wide range of cryogenic or elevated temperatures.

Busch (1926) found that symmetric Electric and Magnetic fields can act as a particle lens and Broglie et al. (2007) developed the concept of corpuscle wave. Equation (1) gives the wavelength of an electron:

$$\lambda = \frac{h}{p} = \frac{h}{m_o v} = \frac{h}{\sqrt{2m_0 eU}} = \frac{1}{\sqrt{1+\frac{eU}{2m_0 c^2}}} \quad (1)$$

Where, λ – Electron wavelength, m; h – Planck's constant, about 6.6×10^{-34} m^2·kg/s; m_0 – Mass of an electron, about 9.1×10^{-31} kg; e – Electron charge, about 1.6×10^{-19} C; c – Speed of light, about 3.0×10^{8} m/s; U – Electric potential of the source, V.

Scanning a beam of electrons, SEM focuses on a fine spot (as small as 1 nano-meter in diameter) across the surface of the sample. As a result of the interaction, various types of signals are generated, including secondary electrons (SE), characteristic X-rays and light (CL), reflected or back-scattered electrons (BSE), and absorbed current and transmitted electrons. Fig. 2-1 shows the mechanisms of different signals and PE means the primary electron.

All these signals can be measured and monitored through detectors to form an image. Different signals can reveal different information of the sample: (1) SE: the secondary electrons are emitted in the very close distance with the sample surface. The number of electrons, which depends on the specimen topography, can be detected. By scanning the sample and collecting the secondary electrons that are emitted using the special detector, a high-resolution image of the sample surface can be produced. The details can be 1 nm in size. (2) BSE: the reflected or back-scattered electrons are beams reflected from the sample by elastic scattering. They occur from deeper locations of the specimens compared with the locations of SE, which lead to less resolution of BSE images. However, because of the strong relation to the atomic number of the specimen, associated with spectra from the characteristic X-rays, BSE signals are always used in the analytical SEM. The result images can provide information about the distribution of different elements in the sample. (3) Characteristic X-rays: the X-ray signals are emitted when the electron beam removes an inner shell electron from the sample, generating higher-energy electron to fill the shell and release energy. The signals can be used to identify the composition and measure the abundance of elements in the sample.

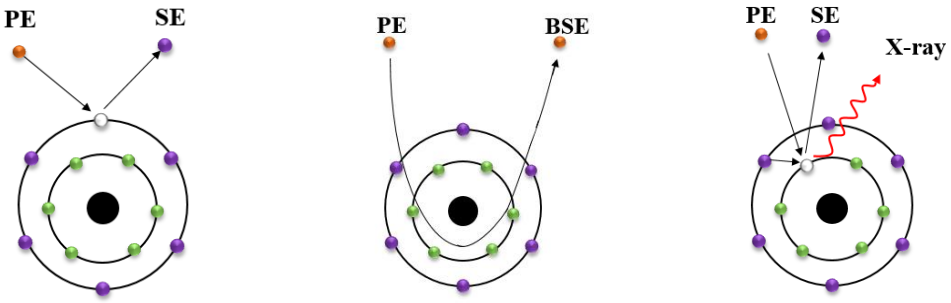

Fig. 2-1 Mechanism of Emission of Different Signals
(a) Secondary Electron; (b) Back-scattered electron; (c) Characteristic X-ray

Secondary electron signal is the most commonly used, and its detectors are standard equipment in all SEMs. However, it is rare that the detectors for all these signals are in one single machine.

In the process of scanning, the SEM creates a focused beam of electrons, using an electron optical column where an electron gun can fire the electrons via an array lens to focus the beam. In this research, the value of electric potential used in rock scanning is about 10 kV and as the calculation of equation (2), means the electron velocity is about 5.94×10^{7} ms^{-1}.

$$v = \sqrt{\frac{2eU}{m_0}} \tag{2}$$

Where v – Velocity of the electron, ms-1; e – Electron charge, about 1.6×10^{-19} C; U – the Electric potential of the source, V; m_0 – Mass of an electron, about 9.1×10^{-31} kg. Because of the high velocity, the electrons would collide with the gas particle, which would render the SEM completely inefficient. As a result, the optical column should maintain different degrees of vacuum throughout the entire device to guarantee the electrons can propagate to the sample, and back to the detector.

The resolution of SEM can achieve sub-nm, which is far higher than the resolution of any other optical devices. The equation (3) defines resolution.

$$2d = \frac{\lambda}{n\sin\theta} = \frac{\lambda}{NA} \tag{3}$$

Where d – Resolution, m; n – Refractive index of the medium; NA – Numerical aperture; θ – Half angle subtended by the objective lens; λ – Electron wavelength, m.

When the interaction of the sample and the primary electron beam happens, because of repeated random scattering and absorption within interaction volume, the electrons lose energy. The interaction volume is a teardrop-shaped volume of the specimen and extends from less than

100 nm to about 5 μm into the surface. The electron's landing energy, the specimen's density, and the atomic number of the specimen decide the size of the interaction volume.

Different with optical and transmission electron microscopes, whose magnification is a function of the power of the objective lens, the SEM has a condenser and objective lenses, whose function is to focus the beam to a spot, not to image the specimen. The SEM can control its magnification over a range of about 6 orders, from about 10 to 500,000 times. For an SEM in the scanning probe microscope, the ratio of the dimensions of the raster on the specimen and the raster on the display device result in the magnification. Under the condition of fixed size of the display screen, the reducing size of the raster on the specimen leads to higher magnification results and vice versa. Therefore, it is the current supplied to the x, y scanning coils, or the voltage supplied to the x, y deflector plates, not the objective lens power that controls the magnification.

2.1.2 Self-adaptive Image Enhancement Method

This section includes a well-developed image segmentation algorithm – Otsu's method, a histogram modification algorithm – Incomplete beta function, and an optimization algorithm – Simulated annealing method.

Otsu's Method

Image segmentation is one of the most important image processing techniques, which can extract the objects from the background by selecting a proper threshold of grey level. As an easy and well-developed image segmentation method, Otsu's method is a nonparametric and unsupervised method of automatic threshold selection for image segmentation. Otsu (1987) proposed this method from the viewpoint of discriminant analysis, providing a method to select the optimal threshold automatically and evaluate the "goodness" of the selected threshold.

In this research, the pixels of the images are represented by the grayscale intensity from 0 to 255. Let n_i denote the number of pixels with the grayscale intensity i, and the total number of pixels is $N = \sum n_i$. Normalize the histogram as a probability distribution with equation (4).

$$p_i = \frac{n_i}{N},\ p_i \geq 0 \text{ and } \sum p_i = 1 \tag{4}$$

The pixels in the images can be classified into two categories: C_o as the Objective -- micro-cracks in the scanning images, and C_B as the background or the matrix. The threshold which separates these two categories is k, which means C_o denotes the pixels with grayscale intensity from 0 to k and C_B denotes the pixels with the pixels with grayscale intensity from k+1 to 255. The probability of category occurrence can be given by equation (5) and (6):

$$\omega_o = \sum_{i=0}^{k} p_i \tag{5}$$

$$\omega_B = \sum_{i=k+1}^{255} p_i \tag{6}$$

Correspondingly, the mean grayscale intensity of each category are given by equation (7) and (8) respectively:

$$\mu_o = \sum_{i=0}^{k} iPr(i|C_o) = \sum_{i=0}^{k} \frac{ip_i}{\omega_o} \tag{7}$$

$$\mu_B = \sum_{i=k+1}^{255} iPr(i|C_B) = \sum_{i=k+1}^{255} \frac{ip_i}{\omega_B} \tag{8}$$

ω_o, ω_B and μ_o, μ_B are the zeroth-order and the first-order cumulative moments of the histogram up to k-th grayscale intensity. For any grayscale intensity of k, the following equation (9) can be verified:

$$\omega_o\mu_o + \omega_B\mu_B = \mu_T,\ \omega_o + \omega_B = 1 \tag{9}$$

Where μ_T -- overall mean grayscale value.

The variances of each category, which are the second-order cumulative moments of the histogram, can be given by equation (10) and (11):

$$\sigma_o^2 = \sum_{i=0}^{k}(i-\mu_o)^2 \Pr(i|C_o) = \sum_{i=0}^{k}\frac{(i-\mu_o)^2 p_i}{\omega_o} \tag{10}$$

$$\sigma_B^2 = \sum_{i=k+1}^{255}(i-\mu_B)^2 \Pr(i|C_B) = \sum_{i=k+1}^{255}\frac{(i-\mu_B)^2 p_i}{\omega_B} \tag{11}$$

As the measures in the class separability used in the discriminant analysis (Fukunaga, 2013), the "goodness" evaluation parameters are given by equation (12):

$$\lambda = \frac{\sigma_1^2}{\sigma_2^2}, \qquad \kappa = \frac{\sigma_3^2}{\sigma_2^2}, \qquad \eta = \frac{\sigma_1^2}{\sigma_3^2} \tag{12}$$

Where σ_1^2 -- the within-class variance; σ_2^2 -- the between-class variance; σ_3^2 -- the total variance, which are defined by the equation (13), (14), and (15) respectively:

$$\sigma_1^2 = \omega_o\sigma_o^2 + \omega_B\mu_B^2 \tag{13}$$

$$\begin{aligned}\sigma_2^2 &= \omega_o(\mu_o-\mu_T)^2 + \omega_B(\mu_B-\mu_T)^2 \\ &= \omega_o\omega_B(\mu_o-\mu_B)^2\end{aligned} \tag{14}$$

$$\sigma_3^2 = \sum_{i=0}^{255}(i-\mu_T)^2 p_i \tag{15}$$

Then the problem of selecting the best threshold of grayscale intensity has been transferred to an optimization problem of the threshold to make one of the "goodness" parameters maximum. From the basic relations among the evaluation parameters, given by equation (16), these three evaluation parameters are not independent.

$$\kappa = \lambda + 1, \quad \eta = \frac{\lambda}{\lambda+1} \tag{16}$$

Maximizing one of the evaluation parameters means maximizing all the evaluation parameters. It is noticed that the within-class variance and the between-class variance depend on the selection

of threshold value, but the total variance does not. Also, the within-variance is based on the second-order statistical property, and the between-class variance is based on the first-order statistical property. As a result, η is the simplest and best parameter to evaluate the "goodness" of the threshold value selection.

Based on the equation (14), for the possible range of optimal threshold value ([0, 255]), the optimal threshold value must exist. Because $\omega_o \geq 0$ and $\omega_B \geq 0$, the minimum value of the between-class variance is 0 when k = 0 and k = 255, or all pixels belong to one single category. Search all the threshold value and select the optimal k value – $k_{optimal}$, which makes η maximum, and equivalently makes the within-class variance maximum, described by equation (17).

$$\sigma_2^2(k_{optimal}) = \max[\sigma_2^2(k)], 0 \leq k \leq 255 \quad (17)$$

From the introduction of Otsu's method, for the ideal case of image segmentation using this method, there should be a sharp and deep valley between the two peaks in the grayscale intensity histogram, which stands for the object and background respectively. But for most of the cases, the valleys are broad and flat, even imbued with noise or the two peaks are extremely unequal in height, which causes that it is difficult to detect the valley bottom precisely.

Incomplete Beta Function

The incomplete beta function is one of the histogram modification operators, which belongs to the image enhancement techniques. The purpose of image enhancement is to improve the image quality and in this research, to enhance the contrast between target and background, which improve the chance of success image segmentation finally.

For histogram modification techniques, the basic procedure can be summarized as: Let $G = \{g_{ij}\}$ denote the original image, where g_{ij} denotes the grayscale intensity at the pixel (i, j). The

objective of the transformed operator $g'_{ij} = F(g_{ij})$ to rescale the grayscale intensity histogram. The incomplete beta function is context-sensitive because it depends on the original image G. Some researchers used different parametric functions to operate the modification procedure: Cocklin et al. (1983) used a finite Rayleigh distribution, which is a special class of the gamma distribution function and Wang et al. (1983) used the regular gamma function. Although these functions allow for the variable shape of the histogram of the grayscale value and determined by the pre-set parameters, these functions are positive on the positive real line, which means truncation is needed to fit the grayscale value.

Tubbs (1987) proposed the incomplete beta function as transformed operator of the grayscale value distribution curve in 1987. Equation (18) is the probability density function:

$$f(u) = \frac{u^{\alpha}(1-u)^{\beta-1}}{B(\alpha,\beta)} \tag{18}$$

Where, $u = \frac{g_{ij-L}}{U-L}$; U – Upper limit of the grayscale intensity, 255; L – Lower limit of the grayscale intensity, 0; $0 \leq u \leq 1$, $\alpha > 0$, $\beta > 0$, and $B(\alpha, \beta) = \frac{\Gamma(\alpha)\Gamma(\beta)}{\Gamma(\alpha+\beta)}$.

Based on equation (18), the definition of the incomplete beta function is given by equation (19):

$$F(u, \alpha, \beta) = \frac{\int_0^u x^{\alpha-1}(1-x)^{\beta-1}dx}{B(\alpha,\beta)} \tag{19}$$

There are two parameters to determine this transformed operator:α and β. Different values of α and β will lead to different function curve. Fig. 2-2 shows the curve shape for different α and β values.

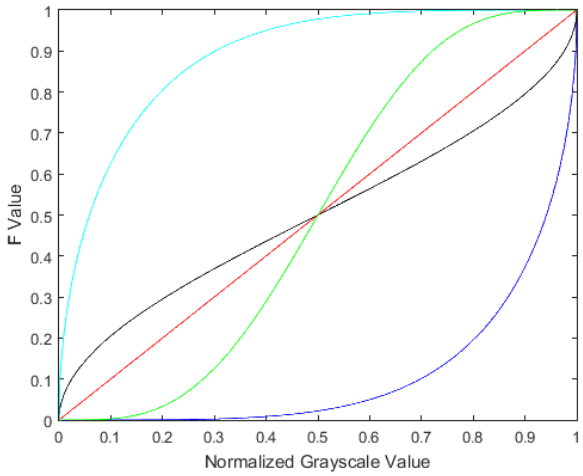

Fig. 2-2 Incomplete Beta Function Curve with Different α,β Values
(Blue: $\alpha > \beta$; Green: $\alpha = \beta = 0.5$; Red: $\alpha = \beta = 1$; Green: $\alpha = \beta > 1$; Cyan: $\alpha < \beta$)

The influence of α, β on the incomplete beta transformed curve can be described briefly:

1. $\alpha = \beta = 1$, the transformed curve is a straight line, passing (0, 0) and (1, 1);

2. $\alpha = \beta > 1$, the transformed curve is an 'S' shaped curve, passing (0, 0), (1, 1), and (0.5, 0.5).

3. $\alpha = \beta < 1$, the transformed curve is a reverse 'S' shaped curve, passing (0, 0), (1, 1), and (0.5, 0.5).

4. $\alpha < \beta$, the transformed curve is upward-bulged, passing (0, 0) and (1, 1). The operator will amplify the contrast at lower grayscale value range.

5. $\alpha > \beta$, the transformed curve is downward-bulged, passing (0, 0) and (1, 1). The operator will amplify the contrast at higher grayscale value range.

Simulated Annealing Algorithm

After analyzing the characteristics of incomplete beta function, the problem is transferred to a combinatorial optimization, whose aim is to find the extreme values of a function of multi-

variables. The simulated annealing method, which was proposed by Kirkpatrick et al. (1983), provides a possible solution for this optimization problem. The key point of the simulated annealing method is an analogy with thermodynamics, specifically with the way liquids freeze and crystallize, or metals cool and anneal. At high temperature, the molecules can move freely, and when the temperature is lowered slowly, the molecules line up in crystals gradually, which means the system is reaching the minimum energy state. Because of the enormous number of molecules in any natural system, only the most probable behaviour of the system in thermal equilibrium at a given temperature can be observed (Deutsch & Journel, 1994; Metropolis et al., 1953). The phenomena can be characterized by the average and small fluctuations about the average behaviour of the system when the average is taken over the ensemble of identical systems introduced by Gibbs. The free energy can be presented by equation (20):

$$E = E_I - TS \tag{20}$$

Where E_I – Internal Energy; T – Temperature; S – Entropy.

In this ensemble, each configuration, defined by the set of molecule positions – $\{r_i\}$, of the system is weighted by its Boltzmann probability factor – $\exp(\frac{-E\{r_i\}}{k_B T})$, where $E\{r_i\}$ stands for the energy of the system, k_B – Boltzmann's constant, and T – System temperature.

The decrease of E and increase of S are beneficial factors to reduce the free energy of the system. With different T, the weight of these two factors is different: At higher temperature, the change of entropy is dominating; At the lower temperature, the change of internal energy takes over. Also, for a faster simulation process, Metropolis et al. (1953) proposed that in every step, the 'molecule' can be given a small displacement, and if the displacement leads to lower energy, the

displacement is accepted 100%. If the energy increases, it is accepted with a probability, which decreases with the decrease of temperature.

Correspondingly, the procedure and the parameters used in the simulated annealing method of this paper can be described as:

1. Initialize the parameters:

The initial temperature – T_0, 1500 °C; Initial acceptance probability – P_0, 0.9; Cooling parameter – C, 0.85; Maximum iteration step – N, 35; Maximum iteration numbers in one step – M, 1600; Initial value of $\alpha = 1$ with bound of [0.5, 10] and $\beta = 1$ with bound of [0.5, 10].

2. Disturb the system:

Generate the disturbance to the solution and calculate the objective function. The difference of objective function after the disturbance: $\Delta f = f_{new} - f_{old}$. There are two possible conditions:

a. If $\Delta f < 0$, the new solution will be accepted and it is the starting point for the next iteration step.

b. If $\Delta f > 0$, the new solution will be accepted with an acceptance probability, which is defined by equation (21):

$$P = e^{-\frac{\Delta f}{K_B T}} \tag{21}$$

Where k_B – Boltzmann Constant; T – Temperature. Because Δf is always positive, with the decrease of T, the acceptance probability will decrease. Repeat this step until the maximum iteration numbers in one step M is achieved.

3. Lower the temperature:

The ending point of the last step is the starting point for the new step and $T_{k+1} = T_k \times C$, which make the acceptance probability lower and lower. Repeat step 2 until the simulation is over.

4. Stop the simulation:

If one of these two conditions is satisfied, stop the iteration and output the best α, β values:

a. Maximum iteration number N is achieved;

b. The difference between two steps is close enough to 0.

Operate the simulated annealing method and select the evaluation parameter η, mentioned in equation (16), as the objective function.

2.2 X-ray Computed Tomography and Multi-stage Image Segmentation

This section focuses on the X-ray Computed Tomography scanning and image segmentation. This chapter aims to quantify the geometric parameters of the hydraulic fractures in cores from Bakken Formation. Section 2.2.1 introduces the basic knowledge of X-ray computed tomography. Section 2.2.2 explains the methods used in multi-stage image segmentation method, including entropy-based mask method, indicator kriging method, and Hessian fracture filtering.

2.2.1 Introduction to X-ray Computed Tomography

From the second-generation medical CT, which uses multiple detectors in a translate/rotate configuration, to the fourth-generation medical CT, which uses a fan-beam geometry with source rotating within a fixed ring of high-efficiency detectors, they are satisfactory for petroleum engineering applications because they have adequate X-ray energy and dose for scanning core material (Wellington & Vinegar, 1987). The basic quantity measured in each pixel of a CT image is the linear attenuation coefficient --μ, which is defined by equation (22):

$$\frac{I}{I_0} = \exp(-\mu h) \tag{22}$$

Where, I_0 – The incident X-ray intensity; I – The intensity remaining after the X-ray passes through a target. The linear attenuation coefficient depends on both electron density (bulk density) -- ρ and atomic number -- Z, which can be presented by equation (23):

$$\mu = \rho(a + \frac{bZ^{3.8}}{E^{3.2}}) \tag{23}$$

Where a – nearly energy-independent coefficient called the Klein-Nishina coefficient; b – constant. The first term of equation (23) represents Compton scattering, which is predominant at X-ray energies (about 100 kV) where medical CT scanners normally operate. The second term of equation (23) is the photoelectric absorption, which is more important at X-ray energies well below 100 kV.

One image proportional only to bulk density and another proportional only to the atomic number can be obtained by scanning at high and low X-ray energies and solving equation (23) on a pixel basis. Dual-energy CT scanning is achieved by a change in the acceleration voltage applied to the X-ray tube, by X-ray filters placed in the beam, or by a combination of these methods.

When a mixture of atomic species is present, the photoelectric absorption is proportional to the effective atomic number -- Z_e, which is defined by equation (24):

$$Z_e = (\sum f_i Z_i^{3.8})^{1/3.8} \tag{24}$$

Where f_i – The fraction of electrons on the ith atomic number species. From the equation, the effective atomic number measured by CT is heavily weighted towards components of the higher atomic number. It is worth mentioning that the strong dependence of photoelectric absorption on the atomic number can be used to enhance the attenuation contrast between multiple fluid phases and thus improve the accuracy of saturation determination.

CT attenuation data are normally presented on a standardized scale called Hounsfield units that are defined by air at -1000 H and water at 0 H. Thus, each Hounsfield unit represents a 0.1 % change in density. For CT measurement on rock sample, it is more convenient to calibrate and to apply beam-hardening corrections with a SiO_2 standard, such as fused quartz (bulk density = 2.20 g/cm3). A change of ± 1 H is thus equivalent to a fractional density change of $\pm 0.5 \times 10^{-3}$ $(\frac{\Delta\rho}{\rho})$ for the rock sample. A similar procedure with appropriate standards and beam-hardening corrections is used to calibrate the density scale for different samples of rock type. All the CT scanner have some beam-hardening corrections to compensate for the preferential absorption of the low-energy portion of the X-ray beam spectrum as it traverses the object. CT image can be reconstructed from sequential cross-sectional slices taken as the sample is moved through the scanner.

2.2.2 Multi-stage Image Segmentation Method

This section includes the methods or the theories used in the multi-stage image segmentation method: entropy-based masking technique, indicator kriging estimation, and Hessian fracture filtering.

Entropy-based Mask

For dealing with the represented information, the information theory provides basic tools – Entropy function (Shannon, 1948), to quantify a region's information represented by expected value. For an 8-bit grayscale image, each pixel contains any number from 0 to 255 or for 16the -bit grayscale image, each pixel contains any number from 0 to 65535. Based on the assumption (Gonzalez & Woods, 2002) that the intensity of all the pixels of all the pixels is statistically independent, the amount of information using the relative frequency of intensity occurrence in the

image is estimated. Equation (25) defines the entropy, which is the average of the information at a given region.

$$H = -\sum_{i=1}^{n} p(i)\log_2 p(i) \quad (25)$$

Where, $p(i)$ – The relative frequency of intensity occurrence in the region of an image, which is termed as the entropy-estimating window; n – the number of intensity occurrence in the window.

The basic idea of entropy-based masking method is to select the pixels with more information than the others. For a given pixel, the window around is first defined by considering a square neighbourhood, whose size is N×N, depending on the thickness of the feature. The entropy of each window is calculated using equation (25) and assigned to the central pixel of the window. Also, for the pixels around the boundary of the image, the symmetric padding is used to avoid that the window cover beyond the image and the padded values are based on the mirror reflections of a sub-image inside the window, located either in the horizontal or vertical direction, or both of them.

Higher entropy indicats that the intensity of pixels inside the window is more randomly distributed, which means that intensity values change greatly inside the window. Therefore, the pixel with a higher entropy value may be located close to a boundary between void and matrix phase.

One of the most important statistical distribution – Gaussian distribution is used to select important pixels. First, calculate the entropy values of all the pixels and represent them with an entropy histogram. Then the distribution of entropy values is determined using a Gaussian distribution. The reason for using Gaussian distribution is because its easy operation and other statistical distribution can also be used. Last, the pixel with the entropy of two deviations away from the mean, corresponding to the top 2.5 % of the high-ranking entropy inside the discrete

distribution, is selected. Also, the appropriate size of the entropy-estimation window can ensure the success of the entropy-based mask method. The purpose of the entropy-based mask method is to extract the border between the objects and the backgrounds, which means the size of the window should be large enough to cover both the objects and the background.

Indicator Kriging Estimation

The theory of regionalized variables is the fundament of the geostatistical methodologies, which states that the attributes within an area exhibit both random and spatially structured properties (Journel & Huijbregts, 1978). The kriging estimation method is an optimal valuation method, which is considered as the best linear unbiased estimator. Estimate and model the sample variograms, which is the function of their separation distance, to quantify the spatial variability of random variables (Antunes & Albuquerque, 2013). The variogram is computed using equation (26):

$$\gamma(h) = \frac{1}{2N(h)}\{\sum_{i=1}^{N(h)}[z(u_i + h) - z(u_i)]^2\} \tag{26}$$

Where $\gamma(h)$ – the variogram for a distance lag h; $N(h)$ – the number of data pairs for that lag h; $z(u_i)$ and $z(u_i + h)$ – the values of the regionalized variable of interest at locations u_i and $u_i + h$ respectively.

Then $\gamma(h)$ will be modelled by different theoretical models, including:

(1) The linear model, as equation (27) shows:

$$\begin{cases} \gamma(h) = \frac{ah^2}{3L^2}(3L - h) & 0 < h < L \\ \gamma(h) = a\left(h - \frac{L}{3}\right) & L \leq h \end{cases} \tag{27}$$

(2) The exponential model, as equation (28) shows:

$$\gamma(h) = C(1 - e^{\frac{-h}{a}}) \tag{28}$$

(3) The logarithmic model, as equation (29) shows:

$$\begin{cases} \gamma(h) = 3\alpha \log_e(h) & h < L \\ \gamma(h) = 3\alpha \left(\log_e \frac{h}{L} + \frac{2}{3} \right) & h > L \end{cases} \tag{29}$$

Also, there are some other theoretical models, such as Gaussian model, spherical model, combination models etc. In this research, only the linear model, the exponential model, and the logarithmic model are considered.

Indicator kriging is a non-parametric geostatistical method for estimation of the probability of exceeding a specific threshold value -- z_k (0.5 in this research), at a given location. In indicator kriging, the stochastic variable – Z(u), is transformed into an indicator variable with a binary distribution, as the equation (30) shows:

$$I(u|z_k) = \begin{cases} 1, & Z(u) > z_k, k = 1,2, \dots, n \\ 0, & Z(u) \leq z_k, k = 1,2, \dots, n \end{cases} \tag{30}$$

The expectation of $I(u, z_k)$, which is determined by n surrounding data, can be calculated by equation (31):

$$E[I(u|z_k)] = Prob\{Z(u) \leq z_k\} \tag{31}$$

Also, the expectation is equal to the value of the conditional cumulative distribution function of Z(u) for a threshold z_k. For an unsampled location -- u_0, the indicator kriging estimation is calculated by equation (32):

$$I^*(u_0|z_k) = \sum_{i=1}^{n} \lambda_i (z_k) I(u_i, z_k) \tag{32}$$

Where $I(u_i, z_k)$ – the values of the indicator at sampled locations, i = 1,2,…,n; λ_i – the weighted of $I(u_i, z_k)$ in the estimation of $I(u_0, z_k)$.

There are two advantages, which are the conditions as well of the estimator: unbiased and minimum estimation error variance, expressed by equation (33) and equation (34):

$$E[I^*(u_0|z_k) - I(u_o|z_k)] = 0 \tag{33}$$

$$Var[I^*(u_0|z_k) - I(u_o|z_k)] = \text{minimum Var.} \tag{34}$$

Fulfil both conditions by computing the weights -- λ_i, which can be solved from the equation (35):

$$\begin{cases} \sum_{i=1}^{n} \lambda_i(z_k)\gamma(u_i, u_j|z_k) - \mu(z_k) = \gamma(u_j, u_0|z_k) \\ \sum_{i=1}^{n} \lambda_i(z_k) = 1 \qquad\qquad i = 1,2,\dots,n \end{cases} \tag{35}$$

Where, μ_k – the Lagrange multiplier; $\gamma(u_i, u_j|z_k)$ – the variogram value between the indicator variables at the sampled location of u_i and u_j; $\gamma(u_j, u_0|z_k)$ – the variogram value between the indicator variables at the sampled location of u_i and the unsampled location of u_0.

Hessian Fracture Filtering

The key point of Hessian fracture filtering is the Hessian matrix (Voorn et al., 2013), which is a 3×3 symmetric matrix for the 3D image, which contains the second order partial derivatives of the input image data I(x, y, z), represented by equation (36):

$$H = \begin{bmatrix} I_{xx} & I_{xy} & I_{xz} \\ I_{yx} & I_{yy} & I_{yz} \\ I_{zx} & I_{zy} & I_{zz} \end{bmatrix} \tag{36}$$

Therefore, the Hessian matrix state the second order structure of intensity variation around each point of the 3D image (Sato et al., 1997). Also, the Hessian matrix can describe the local curvature of the data in a small neighbourhood surrounding each pixel because the second order information can reflect the curvature.

Taking the method of determining the elements of the Hessian matrix into account can interpret above better. A commonly applied approach comes from the linear space, stating that the second derivative of an image can be obtained by convolving the original image with the derivatives of Gaussians. For a single element of the Hessian matrix, the equation (37) can work as an example:

$$I_{xx} = (B \cdot \frac{\partial^2}{\partial x^2} G(x, y, z, s)) \times I(x, y, z) \tag{37}$$

Where, B -- Factor for normalization; s – Factor of scale, in this research, set s = 8; G – Gaussian function. The Gaussian function in one dimension can be defined by equation (38):

$$G(x, s) = C \cdot e^{-\frac{x^2}{2s^2}} \tag{38}$$

Where, C – Factor for normalization. Fig. 2-3 shows the second derivative of this Gaussian function. The second derivative of this Gaussian function represents a probe kernel for contrast in the image. Simply speaking, when operating the convolution of equation (38), the image data I is compared to the probe kernel, which is the second derivative of G. Therefore, the highest positive response which means the peak is 1, is recorded for a dark feature on a brighter background. The high negative response, which means the slope is -1, is recorded for a bright feature on a darker background. Also, the curve with the extreme value is less than 1 or more than -1 reflects the lesser contract features, narrower features, and broader features, which are dependent on the parameters of equation (38).

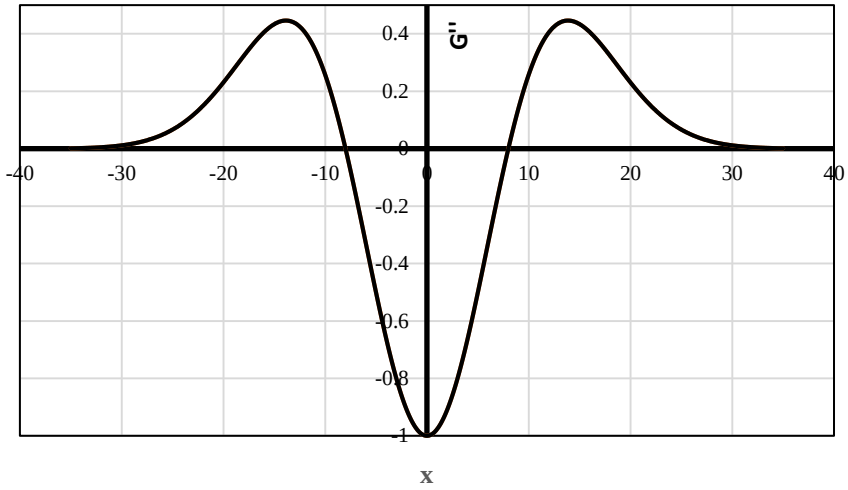

Fig. 2-3 One-dimensional Second Derivative of the Gaussian Curve

The next step is to extend this concept to three dimensions. Operate the convolution in multiple directions, and determine all elements of the Hessian matrix. It is worth noting that the second-order nature of the Hessian matrix makes it invariant to grayscale value offsets, scaling and linear grayscale variations throughout a dataset, which means only the local contrast is assessed, not the actual grayscale value. For example, a feature with grayscale 50 on a background of 100 has the same result with the feature with grayscale value 150 on a background 200.

Then, after the definition of all the Hessian matrix elements, the eigenvectors describing the principal local directions of the curvature, and the eigenvalues describing their magnitude, of the matrix can be determined. The eigenvalues thus represent the magnitude of the largest local contrast change, as well as the magnitudes of the local contrast changes in the other two, orthogonal principal directions (Lorenz et al., 1997). The eigenvalue decomposition of the Hessian matrix can, therefore, be used to distinguish between blob-like, tube-like and plane-like features in a dataset. For the narrow fractures with low intensity on a brighter background, the case should be that one

eigenvalue has a high and positive magnitude, and the other two have a small magnitude. The corresponding eigenvector corresponding to this largest eigenvalue is then the normal to the planar feature.

2.3 Kozeny-Carman Relation

The Kozeny-Carman relation is the most common equation to calculate the permeability from the porosity, the tortuosity, and the grain size. Traditionally, the Kozeny-Carman equation relates the absolute permeability -- k_{ab}, to the porosity -- $\emptyset$ and the grain size – d, as the equation (39) shows:

$$k_{ab} \sim \emptyset^3 d^2 \tag{39}$$

Equation (39) is the classical form, which is frequently employed to mimic the permeability vs porosity evolution. During this calculation, the grain size – d will be kept constant. There are two inconsistencies in this approach: (1) the Kozeny-Carman equation is derived with a solid medium with pipe conduits, rather than with a granular medium; (2) the variation of grain size doesn't affect the results a lot because the porosity almost keeps constant.

Equation (40) defined the basic law of absolute permeability – k_{ab} of porous media (Lorenz et al., 1997; Darcy, 1856):

$$Q = -k_{ab} \frac{A}{\mu} \frac{dP}{dx} \tag{40}$$

Where, Q – the volume flowing through the porous media, m^3/s; A – the cross-sectional area of the porous media, m^2; μ – the dynamic viscosity of fluid Pa·s; dP/dx – the pressure gradient along the direction of fluid flow, Pa/m.

Equation (41) is for laminar viscous flow in a pipe of the radius b:

$$\frac{\partial^2 u}{\partial r^2} + \frac{1}{r} \frac{\partial u}{\partial r} = \frac{1}{\mu} \frac{dP}{dx} \tag{41}$$

Where, u – the velocity of the fluid in the axial direction; μ – the dynamic viscosity of fluid Pa·s; dP/dx – the pressure gradient in the axial direction, Pa/m; r – the radial coordinates; x – the axial coordinates. The general solution of Equation (41) is represented by equation (42):

$$u = A + Br^2 + C + \ln r \tag{42}$$

Where, A, B, and C are constants. Also, A, B, and C will follow the derivative of the equation (42), as the equation (43) and equation (44) show:

$$\frac{\partial u}{\partial r} = 2Br + \frac{C}{r} \tag{43}$$

$$\frac{\partial^2 u}{\partial r^2} = 2B - \frac{C}{r^2} \tag{44}$$

Substitute the expression of equation (44) into equation (42), we get the equation (45):

$$B = \frac{1}{4\mu}\frac{dP}{dx} \tag{45}$$

Another condition is to keep the equation (42) - (44) feasible, which lead to the solution that C = 0. The next step is to employ the boundary condition that there is no slip at the outer boundary, which means u = 0 at r = b. Equation (46) gives the solution of A, and u can be expressed by equation (47):

$$A = -\frac{1}{4\mu}\frac{dP}{dx}b^2 \tag{46}$$

$$u = -\frac{1}{4\mu}\frac{dP}{dx}b^2\left(1 - \frac{r^2}{b^2}\right) \tag{47}$$

Also, the flow volume through the pipe can be expressed by equation (48):

$$q = -\frac{\pi b^4}{8\mu}\frac{\Delta P}{l} \tag{48}$$

Where, l – the length of the pipe; ΔP – the pressure drop along the whole pipe.

Now, assume that the porous phase in the media is made of N identical parallel round pipes embedded in the solid with an angle – α to its horizontal direction. The relationship between the length of each pipe inside the block -- l and the length along the horizontal direction -- L can be expressed by equation (49):

$$l = \frac{L}{\sin\alpha} = L\tau \tag{49}$$

Where, L – the horizontal length of the media; τ – the tortuosity and $\tau = \sin^{-1}\alpha$.

Substitute the equation (49) into equation (48), and obtain equation (50):

$$Q = Nq = -N\frac{\pi b^4}{8\mu}\frac{\Delta P}{L\tau} \tag{50}$$

The porosity can be expressed by the parameters mentioned above, as equation (51) shows:

$$\emptyset = \frac{N\pi b^2 l}{AL} = \frac{N\pi b^2 \tau}{A} \tag{51}$$

Substitute the equation (51) into equation (50), and obtain the equation (51):

$$Q = -\emptyset\frac{b^2}{8\tau^2}\frac{A}{\mu}\frac{\Delta P}{L\tau} \tag{51}$$

Introduce the concept of the specific surface area – s, and it is defined by equation (52):

$$s = \frac{2N\pi bl}{AL} = \frac{2\emptyset}{b} \tag{52}$$

Therefore, the final calculation of absolute permeability expressed by the porosity, the tortuosity, and the specific surface area is as equation (53) shows:

$$k_{ab} = \frac{1}{2}\frac{\emptyset^3}{s^2\tau^2} \tag{53}$$

Kozeny-Carman relation is one of the most classical methods to calculate the permeability of the porous media with simple porous phase. For the case in this research, where the research target is one or two obvious fracture existing in the tight matrix, whose permeability can be ignored (0.04 md on average), the K-C relation can work very well with good accuracy and computational efficiency.

2.4 Data Acquisition and Pre-processing

This section includes the experimental samples, equipment, and procedures. Also, the pre-processing of the input data, mainly about the data selection is also a part of the section. All the contents will be introduced based on different experiments: Section 2.4.1 – High-resolution SEM scanning experiment, section 2.4.2 – X-ray CT scanning experiment and section 2.4.3 – Core-flooding experiment.

2.4.1 High-resolution SEM Scanning Experiment

The research target of the high-resolution SEM scanning experiments are the natural micro-cracks existing in the shale rock samples. There are three rock samples from Upper Bakken shale formation are selected for the scanning experiments, and there are two imaging points for each rock sample, as Fig. 2-4 shows. There are six imaging points: A-a, A-b, B-a, B-b, C-a, and C-b. The procedure of SEM scanning experiment can be explained below:

1. Prepare sample:

(a) There are two sample types in the SEM scanning experiments: conductive and non-conductive. For the non-conductive samples like shale, coat the sample with carbon under 4.2 V for 6 s.

(b) Then secure the sample on a proper sample holder and ground the non-conductive sample with conductive tape.

(c) Use the air spray to clean the sample from dust and other contaminants.

2. Put a sample into the vacuum chamber:

(a) Charge the nitrogen gas into the chamber. Then, open the chamber and secure the sample on the stage when it is ready. Take a top-view image of the sample, which will be used as a reference for the following scanning region selection.

(b) Close the chamber slowly and bring the sample chamber to a high vacuum. In the process of pumping, double-click the user's interest spots to center it on the Nav-cam image. Lift the highest of the sample to the '10 mm'. '10 mm' is set by the user, which can guarantee the safety distance between the sample and the lens.

(c) Set the beam conditions as the recommendation. Click 'Beam On' on the beam page, and click the 'Pause' button on the toolbar. Focus the image by using the final focus knob on the control panel. Click 'link sample Z to working distance' on the toolbar.

3. Optimize output image:

(a) Click the 'Auto-contrast button' to set the best contrast by the system. Then double-click the interesting spot to center it. Click 'Reduced area' on the toolbar to get a small area to optimize image quality, and repeat this step until a high-quality image is obtained. Then, check the dwell time is proper or not. The shorter the dwell time is, the higher the output image will be. Usually, 3 μs is good enough. Also, the brightness and contrast can be adjusted using the corresponding knobs on the control panel.

(b) Use the fine knob on the control panel to get the sharpest image. Use the stigmata X&Y to refine it. Repeat this step until a satisfying image is obtained.

Fig. 2-5 shows the equipment used in this part is FEI Quanta 650 FEG SEM in the IES, UND. The scanning images of the six imaging points are as Fig. 2-6 shows with the resolution of 50 nm.

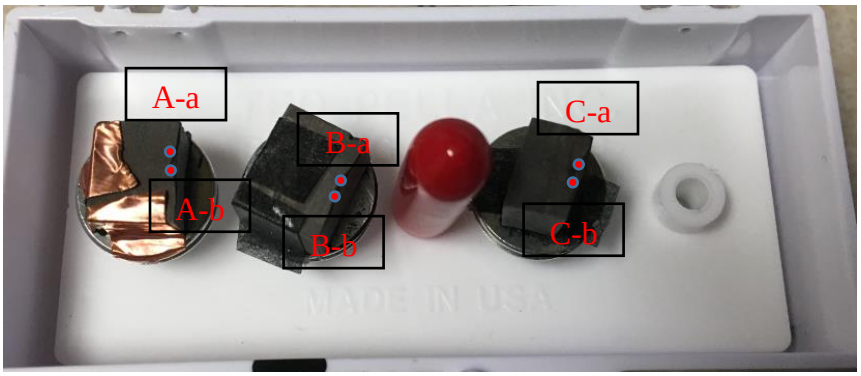

Fig. 2-4 Rock Sample for SEM Experiments (Red points: imaging points)

Fig. 2-5 FEI Quanta 650 FEG SEM

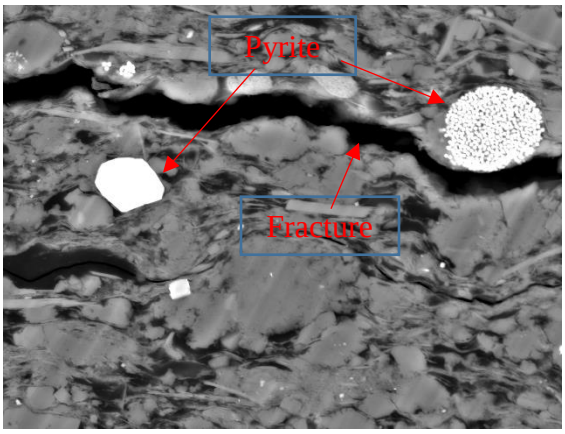

A-a

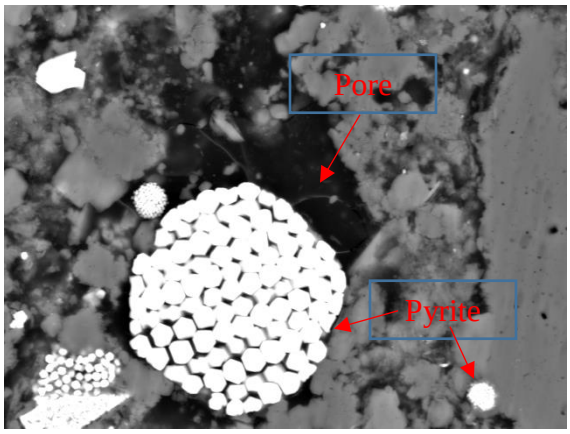

A-b

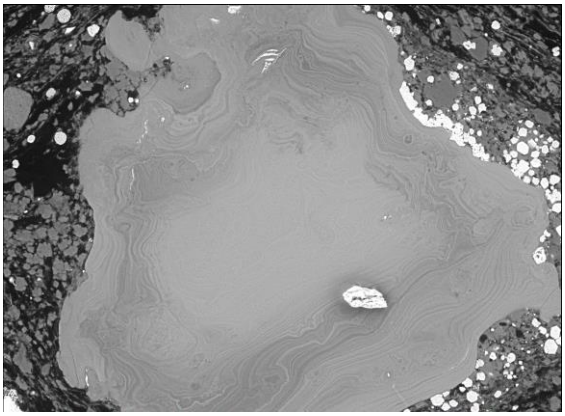

B-a

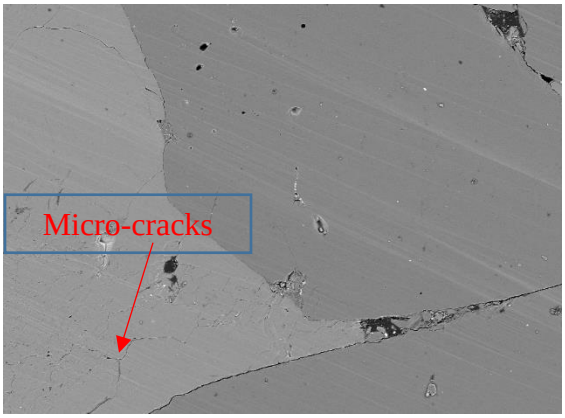

B-b

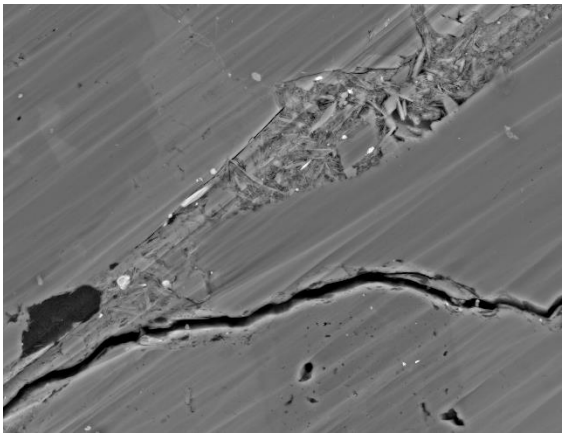

C-a

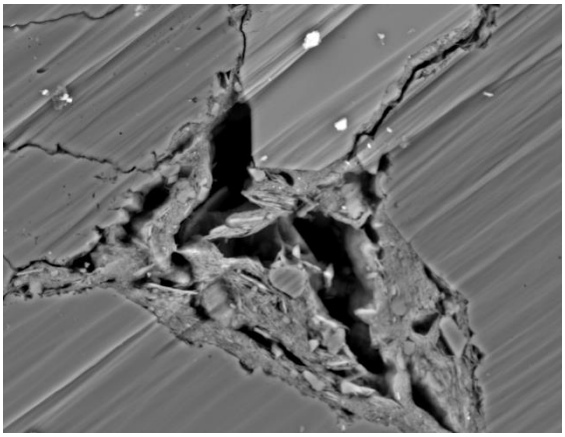

C-b

Fig. 2-6 SEM Scanning Images

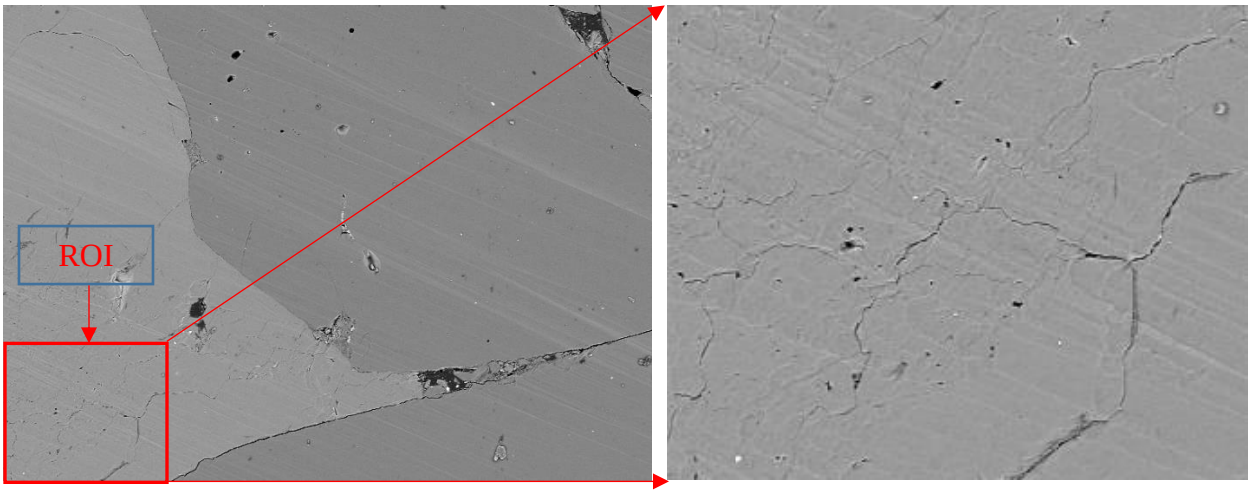

Fig. 2-7 The Region of Interest for Image Enhancement

Fig. 2-6 show the strong function of SEM to reflect the sample surface at nano-scale, including the pore structure, mineral phase (Pyrite commonly), obvious fractures, and micro-cracks. Based on the research target of this part, the image of point B-b is selected, and its region of interest (ROI) is as Fig. 2-7 shows. The selected image and data will be used to operate the image enhancement techniques.

2.4.2 X-ray Computed Tomography Scanning Experiment

The research target of the X-ray CT scanning experiments is the fracture existing in the shale rock samples. There is one rock core after the stimulation treatment from Upper Bakken shale formation, as Fig. 21 (a) shows and Fig. 2-8 (b) shows the X-ray scanning equipment -- GE v|tome|x s microCT in Electron Microscopy Center, NDSU. Fig. 2-9 shows the scanning results in MyVGL.

The three-dimensional images are composed of more than 1,000 two-dimensional images, and the target of the image processing is the two-dimensional images. Fig. 2-10 (a) shows one slice of the two-dimensional images generated by X-ray CT scanning. Because of the boundary effect, there is an obvious noise at the boundary of the rock sample, which will cause errors in the

processing results. Operate the image cropping to cut the noisy region of the image, which is outside the red circle and Fig. 2-10 (b) shows the ROI of Fig. 2-10 (a).

(a) (b)

Fig. 2-8 Rock Core and GE v|tome|x s microCT

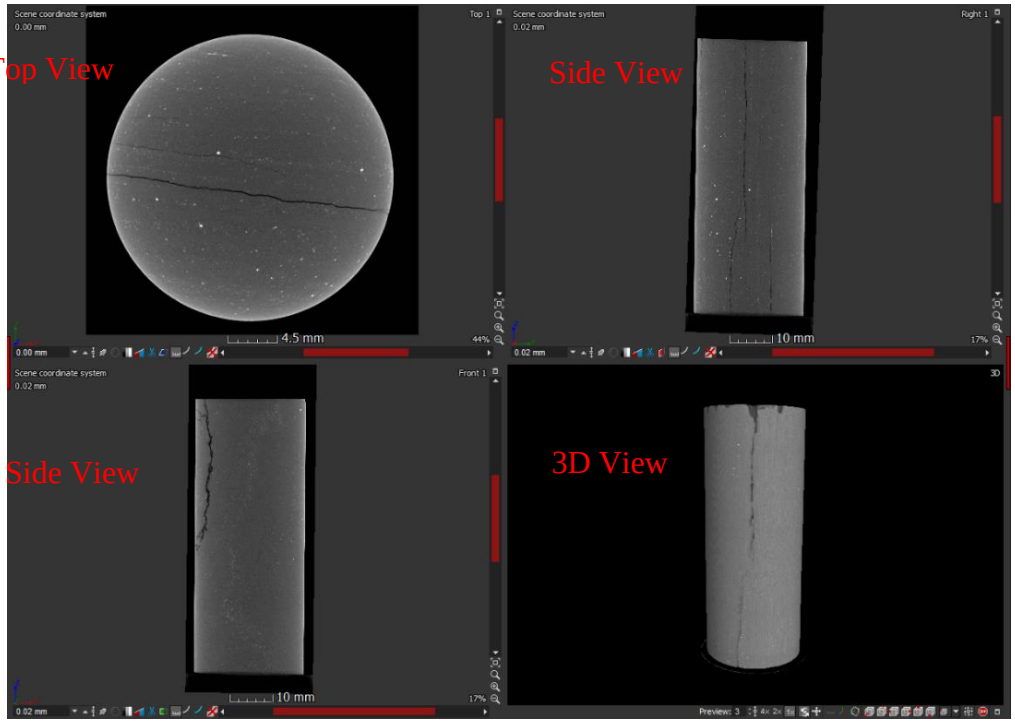

Fig. 2-9 Scanning Result in MyVGL

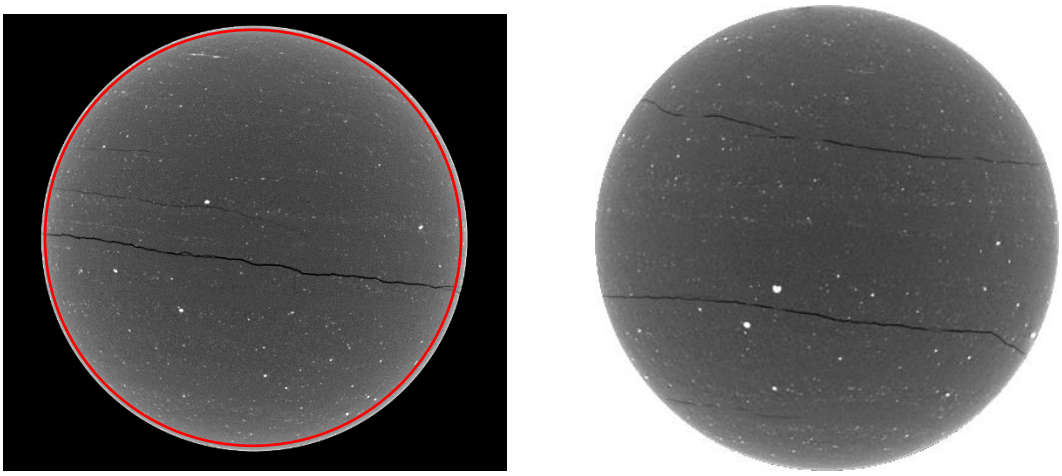

(a) (b)

Fig. 2-10 (a) 2D Slice of 3D Images (b) Region of Interest for Image Segmentation

2.4.3 Core-flooding Experiment

The core-flooding experiment provides an effective way to test the property of the core. It is performed in a triaxial cell, which can enable the core to be tested under the condition required by the user with confining pressures representative of the average stress under hydrostatic conditions. Fig. 2-11 shows the diagram of the core-flooding system (Wang et al., 2018).

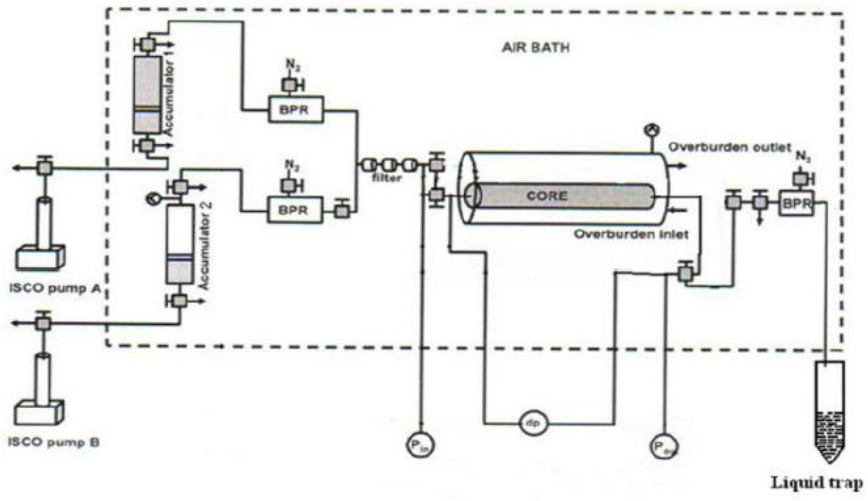

Fig. 2-11 The Schematic diagram of the Core-flooding System

The confining fluid used in the triaxial cell is silicon oil, and the sample is separated with a thin lead foil and then a viton-rubber membrane. Teledyne ISCO 500D syringe pumps are used to control the confining pressure and the gas inflow rates with two pumps used for the flue gas studies involving nitrogen and carbon dioxide injection. The pore pressure was maintained during the core floods using a back pressure control device and the gas rate measured using a Ritter Apparatebau MilliGascounter appropriate for the flow rates associated with the tests.

Because the expected permeability of the fracture is high, and to reduce the influence of the confining pressure on the fracture aperture, set the confining pressure of 400 psi and flow rate of 1 cc/min. The experimental core is the same one used in the X-ray CT scanning experiment. Fig. 2-12 shows the core-flooding equipment in the lab of the Department of Petroleum Engineering, UND.

Fig. 2-12 Core-flooding Experimental Equipment

2.5 Summary

This chapter introduce the basic knowledge of the high-resolution SEM scanning and X-ray CT scanning techniques, about their working principles and major functions. There are two novel image processing methods proposed in this research – Self- adaptive image enhancement method and multi-stage image segmentation method. For self-adaptive image enhancement method, the incomplete beta function is employed to be the transformation operator of the grayscale intensity histogram and the parameter optimization is finished by simulated annealing algorithm. The "Self-adaptive" means the enhancement processes are specifically decided by the input image, not the users. For multi-stage image segmentation method, different with global threshold segmentation method, the usage of entropy-based mask and indicator kriging estimation include the local information in the segmentation process. Also, the experimental equipments, samples and the two-dimensional and three-dimensional result images generated by these scanning techniques are shown in this chapter. These images would be the input data and the processing results would be in Chapter 3.

CHAPTER III

RESULTS & DISCUSSION

This chapter presents the results of image enhancement and image segmentation of the two-dimensional SEM scanning images and three X-ray CT scanning images generated in Chapter 2: Section 3.1 includes the analysis of the histogram intensity histogram, parameter selection results, and the comparison of the segmentation results before and after the image enhancement, which shows the improvement of applying the self-adaptive image enhancement method. Section 3.2 includes the initial image segmentation, the boundary pixel detection, and the final image segmentation. Also, the reconstruction of the three-dimensional model of the rock sample, the core-flooding result, and calculation permeability based on the three-dimensional model using Kozeny-Carman relation are included in section 3.2.

3.1 Two-dimensional SEM Scanning Image Enhancement Results

For Otsu's segmentation method, the separability of features on the grayscale intensity histogram is the most important parameter to evaluate the segmentation performance. Fig. 3-1 shows the original input image and its grayscale intensity histogram. The micro-cracks is not obvious to the naked eyes in Fig. 3-1 (a) compared with the background. From Fig. 3-1 (b), some basic statistical parameter of the input image can be obtained: the mean value is 153.47, and the variance is 107.254, which indicates that the distribution of the grayscale intensity is highly concentrated in the high-value region.

Fig. 3-2 shows the segmentation result of Fig. 3-1 (a) using Otsu's method. There is an obvious insufficient segmentation in Fig. 3-2 The threshold value is 127, which is the red line in Fig. 3-1 (b). Based on that threshold value, the separability evaluation parameter – η, which is described in section 3.1.2, equals 2.148. The segmentation result lost most of the valuable information about micro-cracks.

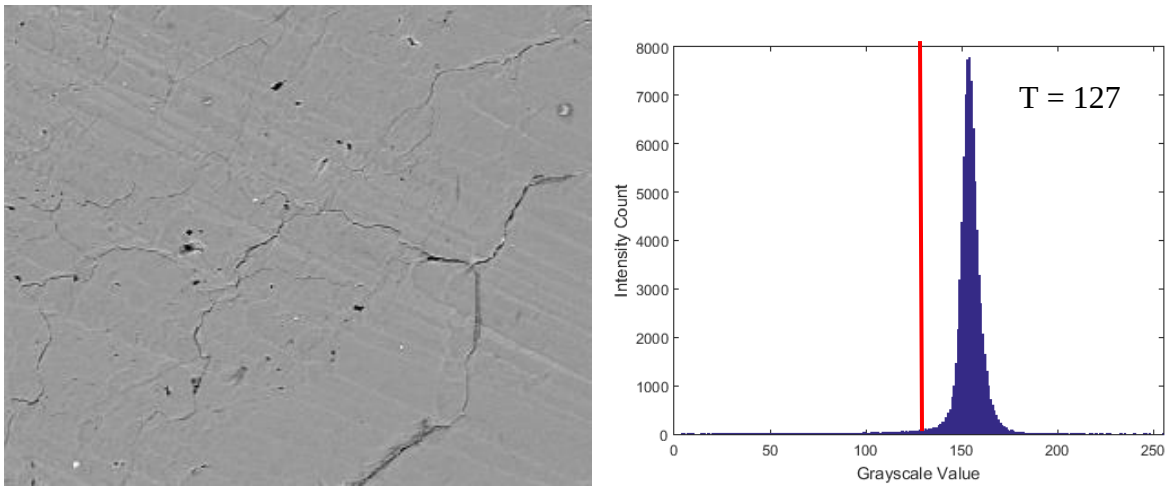

(a) (b)

Fig. 3-1 (a) Input Image (b) Grayscale Intensity Histogram

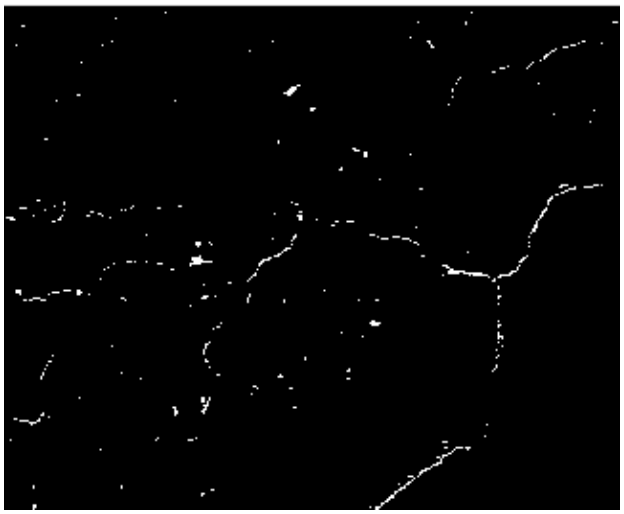

Fig. 3-2 Image Segmentation of Input Image

To improve the image quality for more precise segmentation, operate the image enhancement techniques to the input image. First, operate two well-developed image enhancement methods – Histogram match and histogram equalization. Fig. 3-3 and Fig. 3-4 show the new grayscale intensity histogram and the segmentation result.

From Fig. 3-3, the grayscale intensity histogram is matched by some pre-set distribution. Because the key parameters are determined by the main features of the histogram, the information of the micro-cracks is not that important in the matching process, which lead to the obvious insufficient image segmentation. From Fig. 3-4, the grayscale intensity histogram is equalized into the whole range, from 0 to 255. This method successfully enhance the information of the background but weaken the information of the target, which cause that the target disappears in the segmentation result.

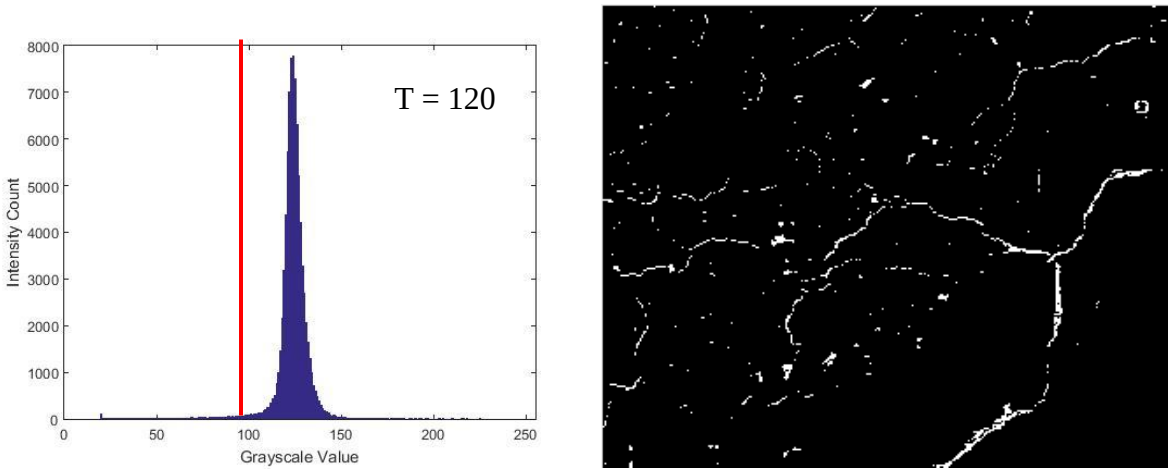

Fig. 3-3 Result of Histogram Match

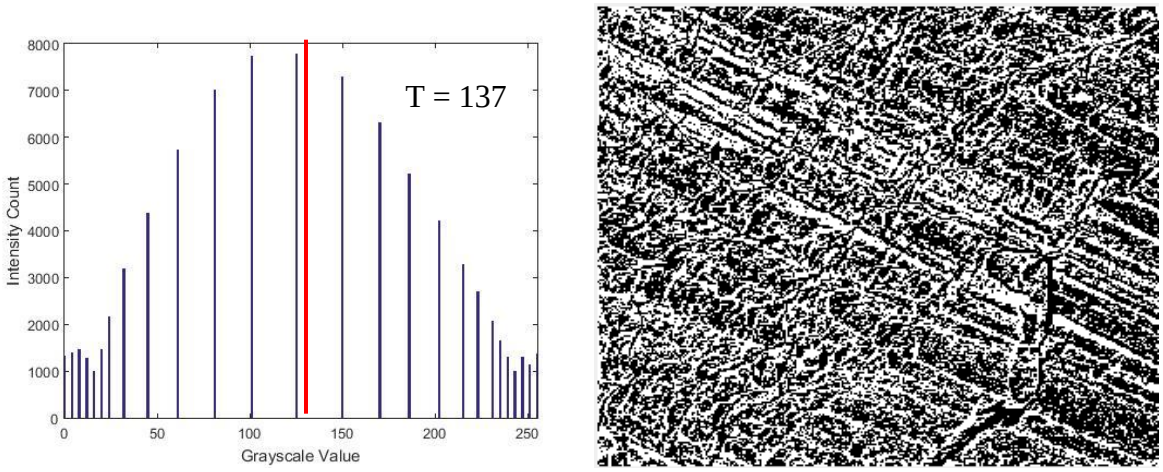

Fig. 3-4 Result of Histogram Equalization

Then, operate the self-adaptive image enhancement method to the input image, from the description in section 2.1.2.2, the key point is the selection of the values of α and β. The optimization algorithm used in this step is the simulated annealing, whose parameters are set as section 2.1.2.3 mentions. Fig. 3-5 shows the result of η with different values of α and β. As a result, The optimal values of α and β, which is 4 and 2 respectively, are selected when the value of η is the maximum, which is 8.6723. Fig. 3-6 shows the optimized transformed curve and the slope of the curve. The comparison of Fig. 3-1 (b) and Fig. 3-6 (b) proves that values of α and β are optimal for the specific input image: the grayscale intensity is concentrated in the range of [130, 180] and the peak of the slope of the transformed curve is also at the same range, which means that the modification of the grayscale intensity histogram is more dramatic than other range and the target, whose grayscale intensity is low, can be enhanced. Fig. 3-7 shows the grayscale intensity histogram and the segmentation result after the self-adaptive image enhancement method. The evaluation parameters of these three image enhancement methods are in Table 3-1.

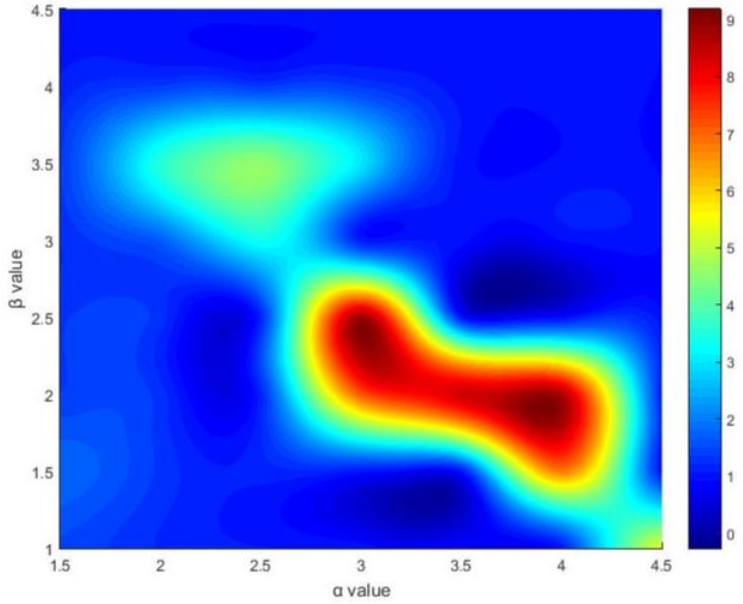

Fig. 3-5 Separability Evaluation Parameters with different values of α and β

(The color intensity stands for the value of η)

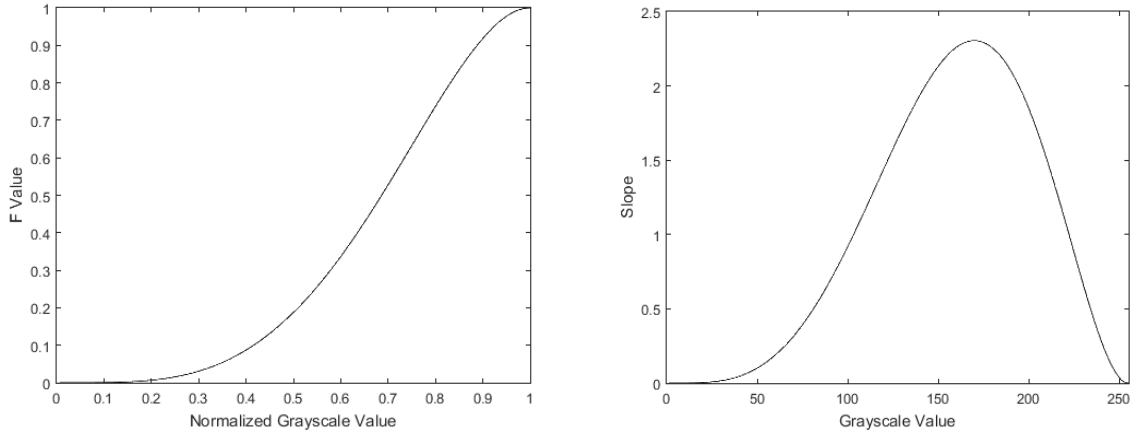

(a) (b)

Fig. 3-6 Separability Evaluation Parameters with different values of α and β

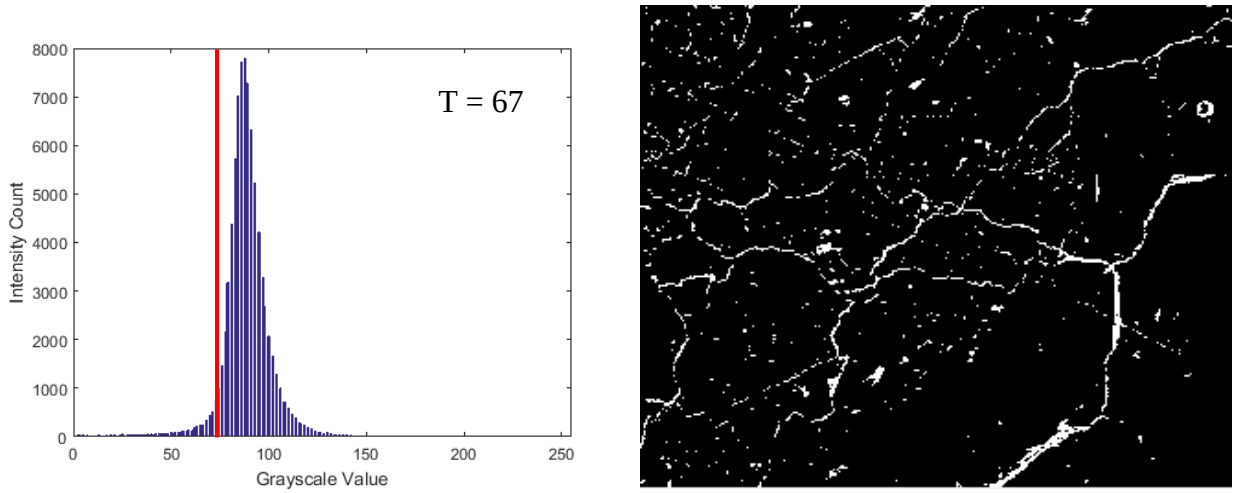

Fig. 3-7 Result of Self-adaptive Image Enhancement

Table 3-1 Evaluation Parameters after Different Image Enhancement

	Original	Histogram Match	Histogram Equalization	Self-adaptive Method
Mean	153.47	123.20	127.12	87.10
Variance	107.254	105.98	55806	117.38
Threshold	127	120	137	67
η	2.1484	3.0156	1.2856	8.6723
Porosity	0.0125	0.0193	0.5419	0.0404

3.2 Three-dimensional X-ray CT Scanning Image Segmentation Results

The three-dimensional X-ray CT scanning image is composed with 1050 two-dimensional images. Fig. 3-8 (a) shows the region of the interest from one slice of two-dimensional image (Slice No.: #4_0241) and Fig. 3-8 (b) shows its grayscale intensity histogram. For the input image shown in Fig. 3-8 (a), the target is not as small as Fig. 3-1 (a), whose information is obvious enough to be reflected in the grayscale intensity histogram.

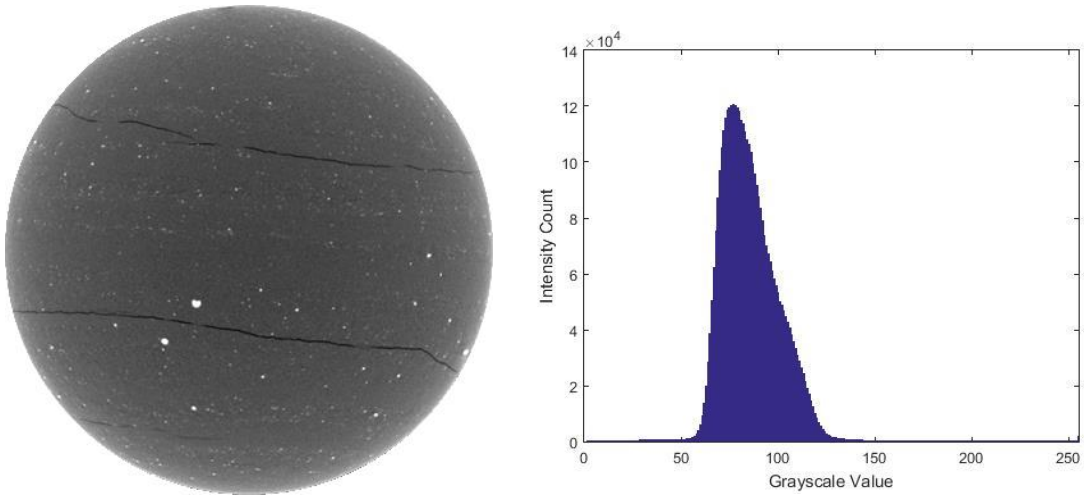

(a) (b)

Fig. 3-8 (a) Input Image (b) Grayscale Intensity Histogram

From Fig. 3-8 (a), the pixels with low-value grayscale intensity represents the porous phase, including the fracture system and the small pores, and the pixels with high-values grayscale intensity represents the mineral phase, including pyrite and silica. Based on that description, the whole image can be divided into three parts: fracture system, matrix, and mineral phase, which obey the Gaussian distribution. The overall distribution of the grayscale value in an image should be the sum of three normal distributions, presenting fracture, matrix and mineral phase separately. For a single phase, set the fitting curve function as equation (54).

$$G_i = a_i \times e^{\frac{(x-\mu_i)^2}{2\sigma_i^2}} \tag{54}$$

Where G – grayscale value; μ – mean value; σ2 – Variance; a – constant coefficient; i – three phases: fracture, matrix, and mineral phase. Using the least square method to calculate the value of all the unknown variables to best fit the frequency distribution of the grayscale value in the cross-section of scanning result. Fig. 3-9 shows the fitting curve. The calculation process can be finished using MATLAB.

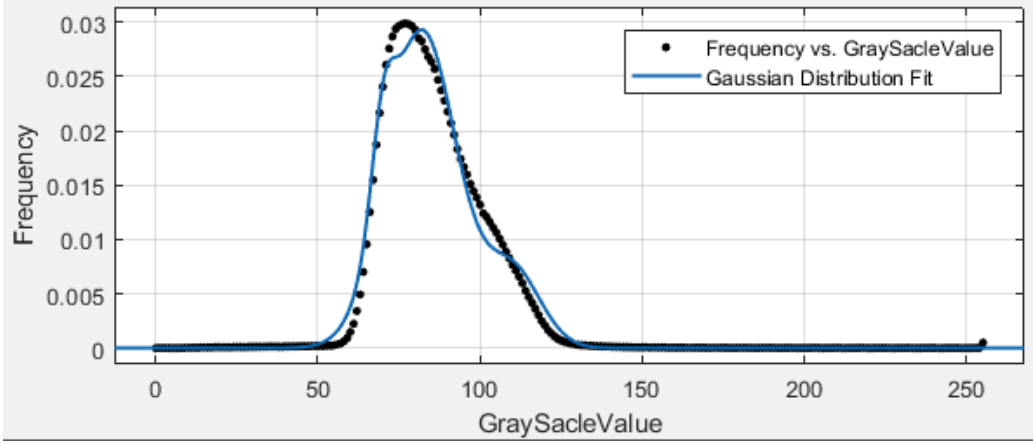

Fig. 3-9 Curve Fitting Result

Curve fitting R-square is 0.9886, which means parameters of three Gaussian distributions to fit the grayscale distribution of the gray image is precise enough. Table 3-2 provides the parameters of the distribution representing fracture system, matrix, and mineral phase. Set the mean values of grayscale intensity distribution as the threshold: The pixels with grayscale below 68 belong to posous phase, and pixels with grayscale intensity greater than 117 belong to mineral phase. The pixels with a grayscale intensity between 68 and 82 belong to either matrix or boundaries of fracture and matrix, and pixels with a grayscale value between 82 and 117, belong to either matrix or boundaries of matrix and mineral phase. Figure 3-10 is the threshold value for initial segmentation. Figure 3-11 is the initial segmentation result of fracture system and mineral phase.

The next step is the boundary pixel detection using entropy function, whose definition is mentioned in section 2.2.2. Set the window size as 9×9 and calculate the entropy of the input image. Fig. 3-12 (a) shows the entropy map of the input image and Fig. 3-12(b) is the entropy value histogram and corresponding normal distribution fitting.

Table 3-2 Normal Distribution Parameters of Different Phases

Phase, i	Constant Coefficient, a	Mean, μ	Variance, σ2
Fracture	0.008646	68	12.76
Matrix	0.02923	82	116
Mineral Phase	0.007076	117	74.2

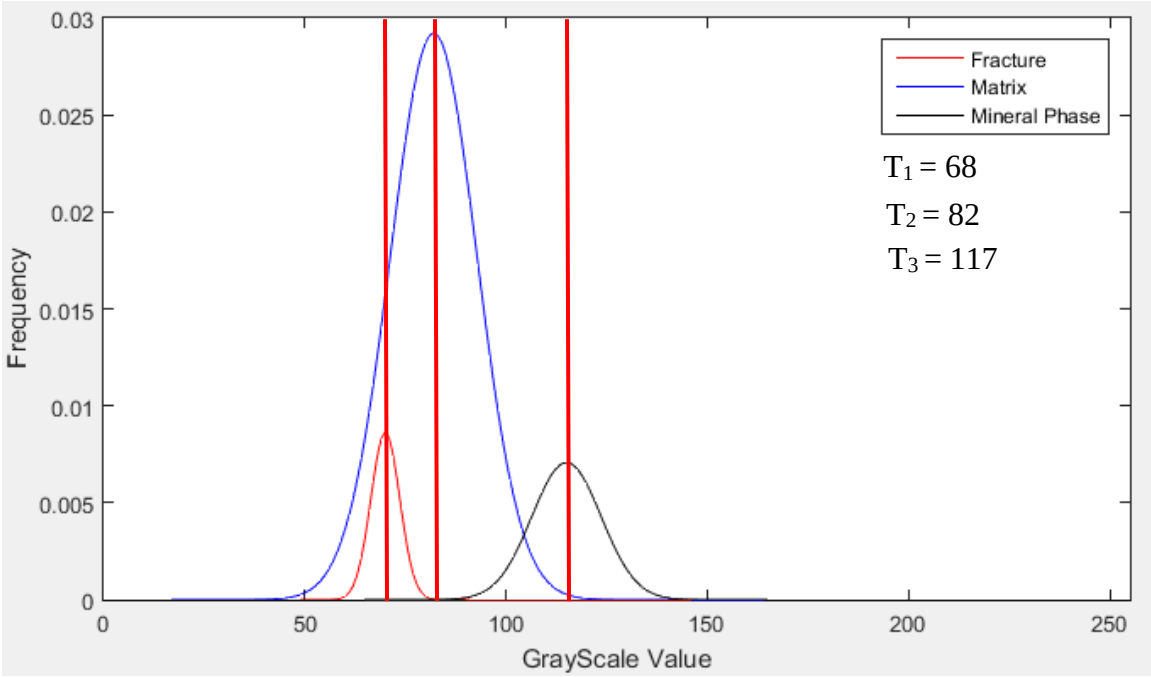

Fig. 3-10 Threshold Value for Initial Segmentation

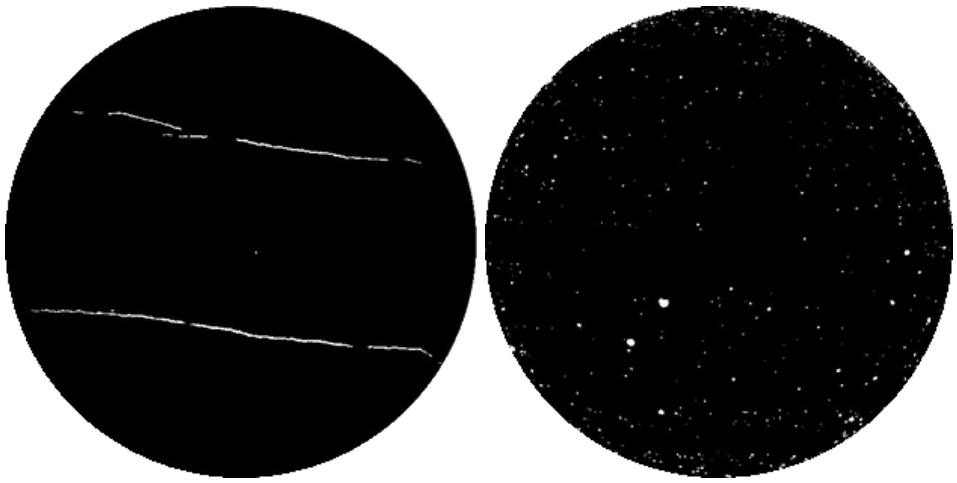

(a) (b)

Fig. 3-11 Initial Image Segmentation Result (a) fracture system (b) Mineral Phase

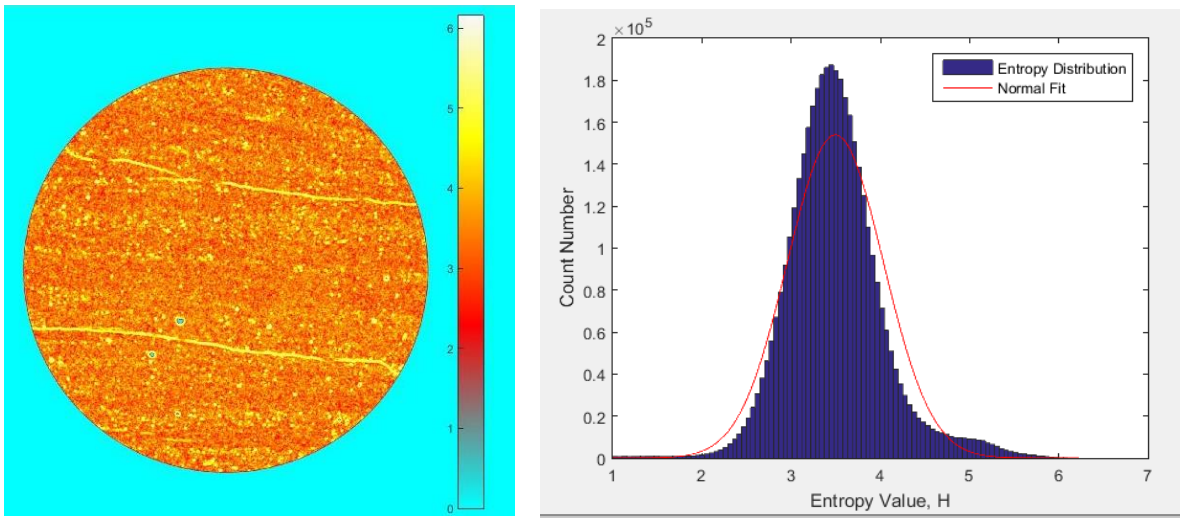

(a) (b)

Fig. 3-12 (a) Entropy Map; (b) Entropy Value Count Distribution and Fitting Curve

The mean and variance of the normal fitting curve are $\mu = 3.5$ and $\sigma^2 = 0.2893$. The pixels with high entropy value are potential boundary pixels. The top 2.5 % is considered as high entropy value, which means the pixels with $H > \mu + 2\sigma = 4.576$ maybe belong to the boundaries between different phases. Fig. 3-13 shows the filtering result. In the result, the white pixels are with $H > 4.576$ (Potential Boundary Pixels) and black pixels are with low-valued entropy.

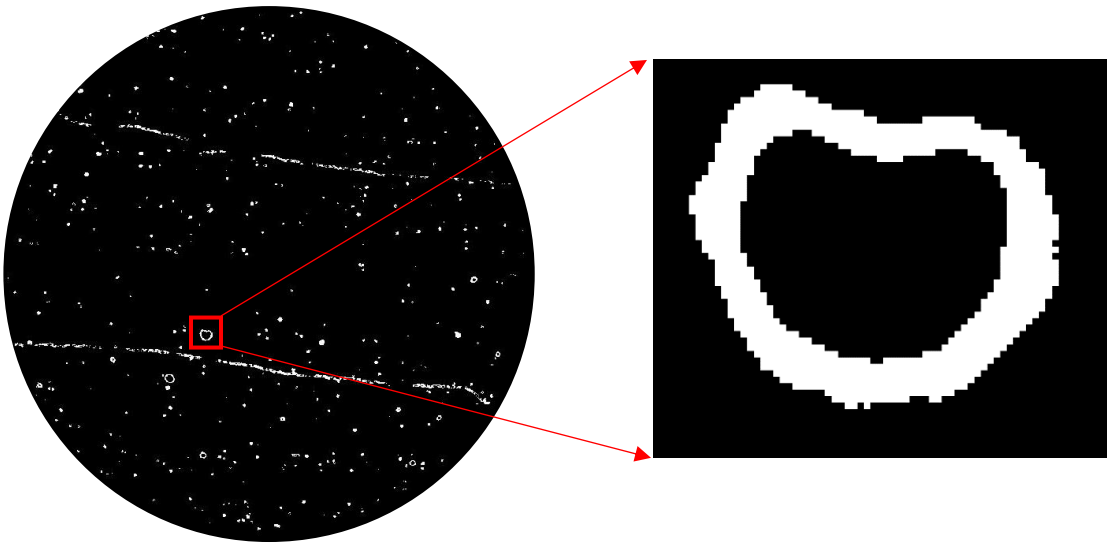

Fig. 3-13 High-value Entropy Filtering Result

Combine the boundary pixel detection results from the initial image segmentation and the high entropy value filtering, Fig. 3-14 shows the boudary pixels between fracture and matrix and Fig. 3-15 shows the boundary pixels between mineral phase and matrix.

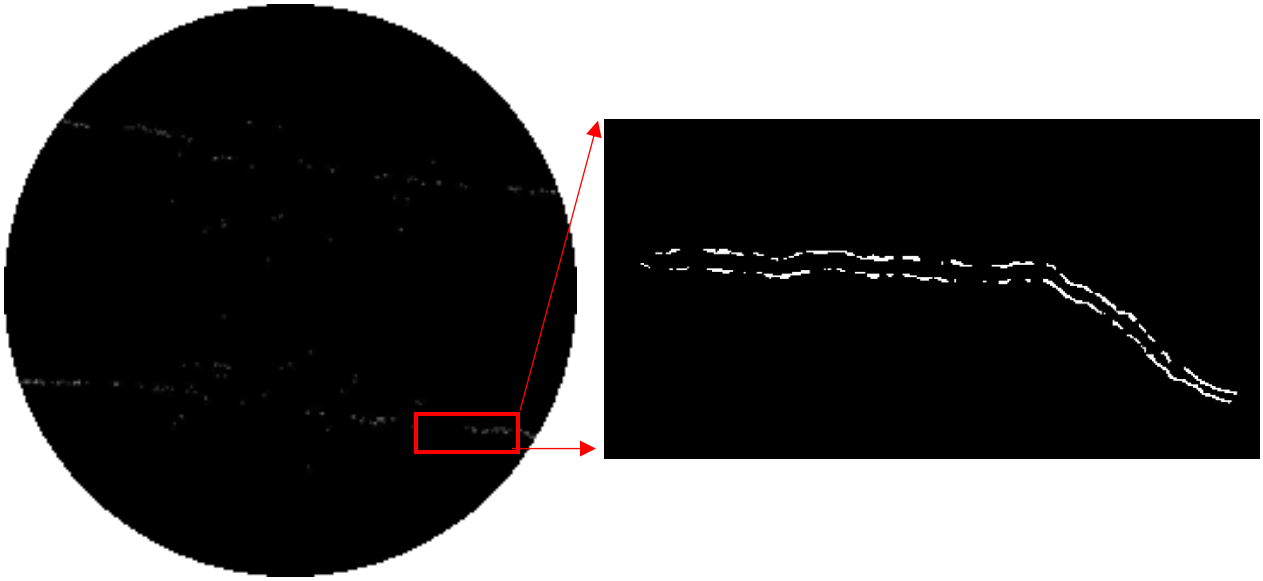

Fig. 3-14 Boundary Pixels between Fracture and Matrix

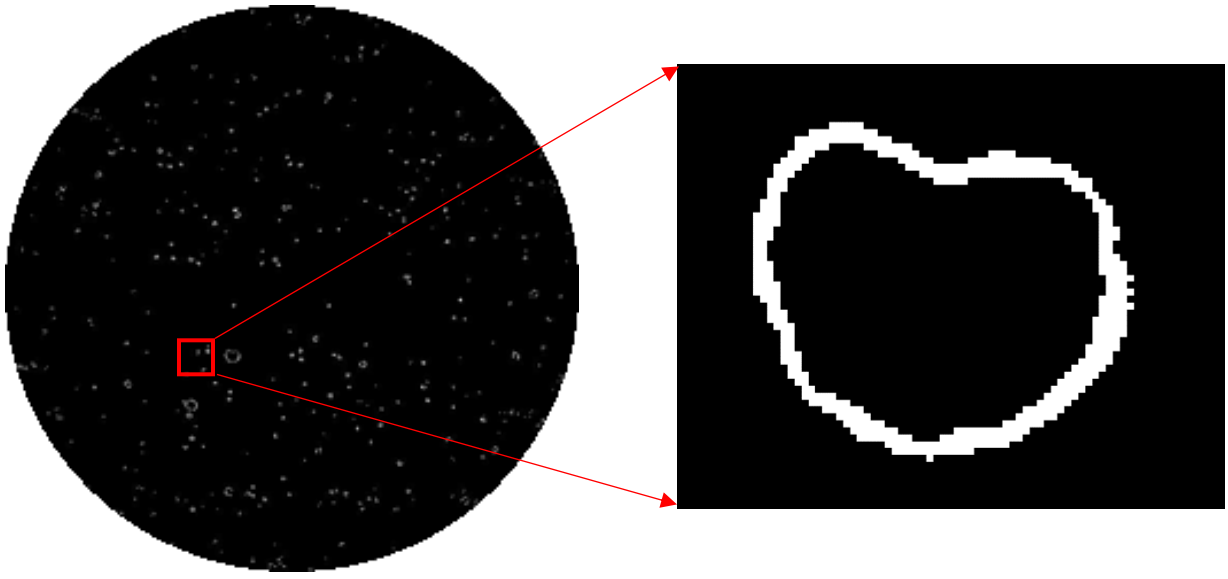

Fig. 3-15 Boundary Pixels between Mineral Phase and Matrix

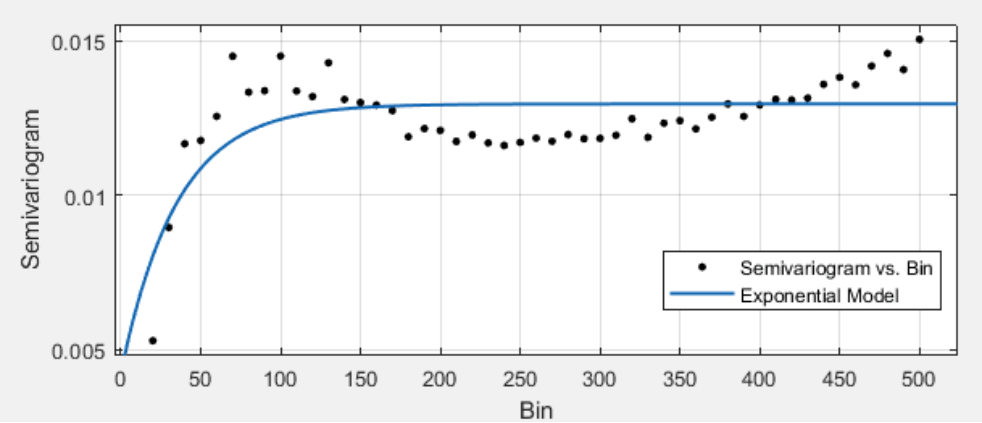

Fig. 3-16 Semivariogram Curve

After the initial segmentation of the gray image and boundary pixel detection, the whole image is divided into two parts: Clearly classified parts, including fracture, matrix and mineral phase; Unclassified part: Boundaries of fracture and matrix, matrix and mineral phase. The next step is to use kriging method, whose theory is explained in section 2.2.2.2, to estimate the classification of the unclassified part. The classified pixels can be used to generate the variogram model. Fig.3-16 shows the semivariogram model of the indicator. Use exponential semivariogram model to fit. The range is about 35-pixel distance.

The model equation is as equation (55) shows:

$$\overline{\gamma}(\mathrm{h}) = 0.004244 + 0.00872 \times (1 - \mathrm{e}^{-\frac{\mathrm{h}}{35}}) \tag{55}$$

where h is the distance between two pixels.

With the kriging result, the boundary pixels can be classified into fracture, matrix and mineral phase and the final segmentation is finished. Repeat this process to all the two-dimensional gray images and generate the three-dimensional models of fracture and mineral phase. Fig. 3-17 shows the top view and the side view of the three-dimensional mineral phase. Fig. 3-18 shows the top view and the side view of the three-dimensional fracture system.

From Fig. 3-17, most of the pyrites are in small aggregates and distributed randomly in the whole rock sample. Also, there are one big aggregate in the bottom half of the rock sample. The volume fraction of the pyrites are about 1.29 %.

From Fig. 3-18, there are three fractures in the rock sample, which are highlighted. Fracture 1 is through the whole rock sample and fracture 2 and 3 are isolated. As a result, only the fracture 1 can serve the function as the flowing channel. The diagram of the fracture systems is shown in Fig. 3-19. Fracture 1 is divided into fracture 1-a and fracture 1-b. Table 3-3 shows the parameters of these three fractures, including length, aperture, horizontal and vertical tortuosity, specific surface area, and porosity.

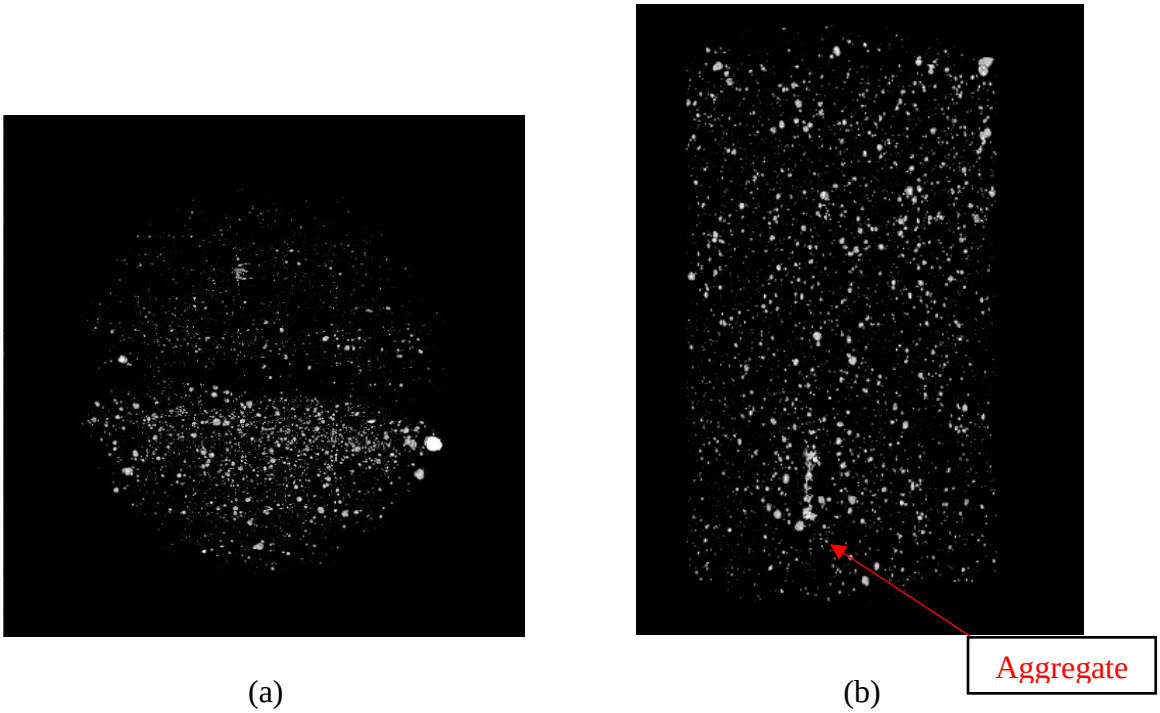

Fig. 3-17 Three-dimensional Image of Mineral Phase (a) Top View of (b) Side View

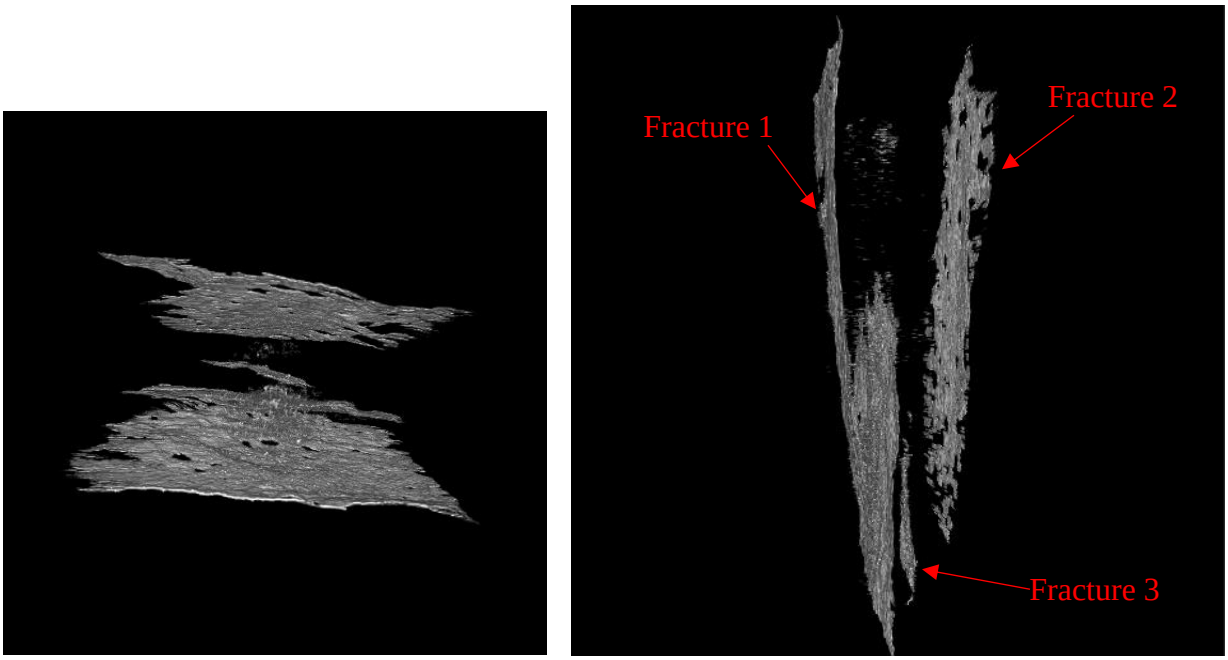

(a) (b)

Fig. 3-18 Three-dimensional Image of Fracture System (a) Top View of (b) Side View

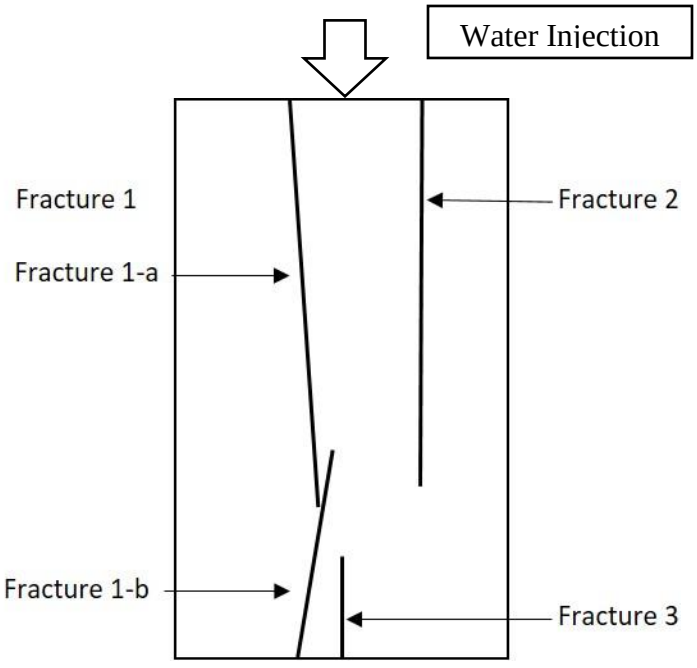

Fig. 3-19 Fracture System Diagram

Table 3-3 Parameters of the Fracture System

	Length/cm	Aperture/μm	Tortuosity	Width/cm	Porosity
Frac. 1-a	4.03	46.4	1.041	2.012	0.25 %
Frac. 1-b	2.95	68.49	1.085	1.613	0.16 %
Frac. 2	3.96	34.6	1.001	1.782	0.19 %
Frac. 3	1.38	16.4	1.001	0.924	0.06 %

Table 3-4 Fracture Parameters from Different Segmentation Method

	Multi-stage Segmentation		Otsu's Method		MHF Filtering	
	Frac. 1-a	Frac. 1-b	Frac. 1-a	Frac. 1-b	Frac. 1-a	Frac. 1-b
Length/cm	4.03	2.95	4.04	2.95	3.99	2.91
Aperture/μm	46.4	68.5	70.2	104.6	22.5	30.8
Tortuosity	1.041	1.085	1.040	1.085	1.035	1.070
Width/cm	2.0	1.52	2.04	1.54	1.89	1.32
Porosity	0.25 %	0.16 %	0.52 %	0.3 %	0.11 %	0.07 %

Calculate the permeability of fracture 1-a and fracture 1-b using Kozeny-Carman relation, which explained in section 2.3. The permeability of fracture 1-a and 1-b is 1080.68 mD and 502.87 mD, respectively. Because the fracture 1-a and 1-b belong to a series system, the fracture of fracture 1 is about 836.47 mD. As the comparison, the parameters calculated from the image segementation using Otsu's method and multi-scale Hessian fracture filtering are shown in Table 3-3.

From Table 3-4, compared with multi-stage segemntation method proposed by this research, the results using Otsu's method show over-segmentation and the results using MHF filtering show insufficient segmentation. Table 3-5 shows the calculated permeability of fracture 1 using different sets of parameters.

Talbe 3-5 Calculated Permeability (mD) using Different Sets of Parameters

	Multi-stage Segmentation	Otsu's Method	MHF Filtering
Frac. 1-a	1080.67	2134.79	533.66
Frac. 1-b	502.87	899.95	284.52
Frac. 1	836.47	1612.72	428.36

The next step is to use core-flooding data to verify the accuracy of processing results using different image segemtation methods. Fig. 3-20 shows the injection pressure with the injection time when the injection rate is 10 cc/min. When the pressure becomes stable, record the pressure value P. For injection rate equals 10 cc/min, the stable injection pressure is 0.0232 MPa. Repeat this process by setting the injection rate as 15, 20, 25, 30, 35, 40 and 50 cc/min and record the table injection pressure. The results are shown in Table 3-6 and Fig. 3-21.

From the Table 3-6 and Fig. 3-20, the core-flooding data shows that the permeability of the rock sample is about 1074.13 mD. The calculated permeability using multi-stage segmentation method is the closest, with the minimum error of 22.1 %.

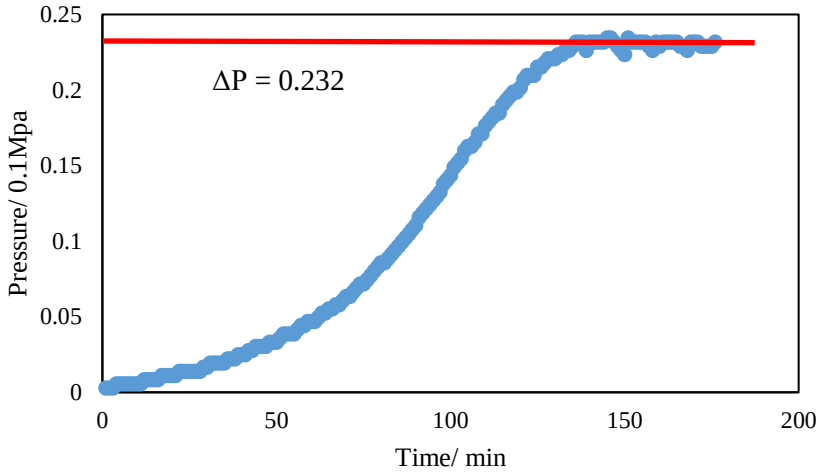

Fig. 3-20 Injection Pressure with Time (Injection Rate = 10 cc/min)

Table 3-6 Stable Injection Pressure with Different Injection Rate

Injection Rate/ cc·min^{-1}	10	15	20	25	30	35	40	50
P/0.1 MPa	0.232	0.355	0.441	0.681	0.689	0.810	1.03	1.10

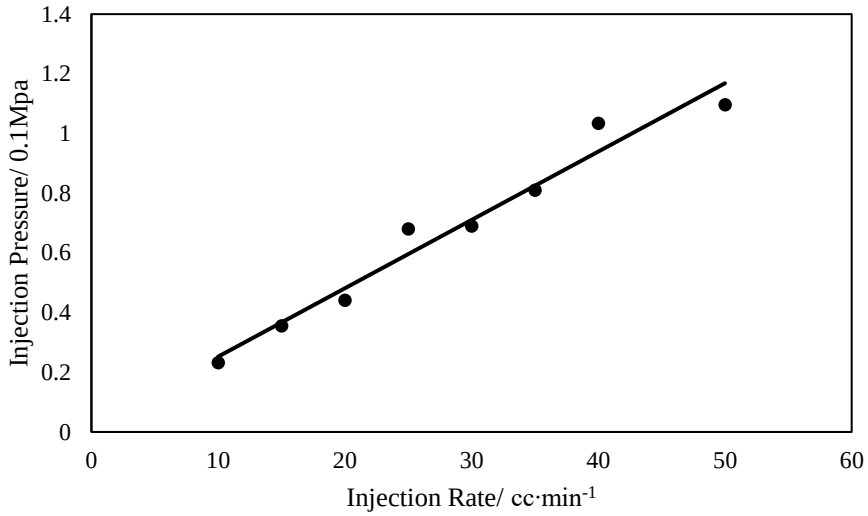

Fig. 3-21 Injection Pressure with Pressure Rate

3.3 Summary

This chapter showed the processing results using self-adaptive image enhancement method and multi-stage image segmentation method step by step.

For the processing result of two-dimensional images, after the image enhancement using incomplete beta function as the transformed operator, the small target becomes more clear to the naked eyes and the information of the target becomes more obvious in the grayscale intensity histogram when comparing Fig. 3-2, 3-3, 3-4 and 3-7. Also, from Table 3-1, the grayscale intensity of the whole image is reduced after the processing, with the mean value reducing from 153.47 to 87.10. The distribution of the grayscale intensity is wider, with the variance increasing from 107.254 to 117.38. Also, the separability of the target and background becomes better, with η increasing from 2.1484 to 8.6723. The precise volume fraction of the micro-cracks is 4.02 %, which is much higher than the original fraction of 1.25 %.

For the processing result of three-dimensional image, from the comparison of the segmentation results using different methods, the results using Otsu's method show obvious over-segmentation because there some noise existing in the scanning images, including the mineral phase, which can increase the threshold value. The results using MHF filtering show insufficient segemtation because this method only consider the fracture satisfyin the pre-set fracture template. The volume fraction of fractures estimated by the multi-stage segmentation (MSS) method is about 0.66 %, with the results from Otsu's method of 1.29 % and MHF filtering 0.30 %. The apertures from MSS of fracture 1-a and 1-b are 46.4 and 68.5 μm, with the results from the Otsu'd method of 70.2 and 104.6 μm, and the results from MHF of 22.5 and 30.9 μm. For the tight rock with the fracture aperture, which is under 100 μm, such difference will lead to big difference in permeability calculation. The permeability calculated from the results using MSS is 836.47 mD, with the error of about +22.1 %, the permeability calculated using Otsu's method is 1612.72 mD, with the error of about +50.1 %, and the permeability calculated using MHF filtering is 428.36 mD, with the error of about -60.1 %. All the comparisons mentioned above show that the multi-stage segmentation method proposed in this research can do a better job of image segmentation.

CHAPTER IV

CONCLUSIONS AND FUTURE WORK

In this research, we proposed two image processing methods – self-adaptive image enhancement method and multi-stage image segmentation method. The experimental samples are the shale rock slices and cores from the Bakken formation. The related theories and detailed methods included in the methods are presented and the processing results of each step are shown and compared with the results using some well-developed methods. The results show that the novel image processing methods proposed in this research have the capability of dealing with the problem of small target segmentation. The key and detailed conclusions of this research are listed below:

(1) The self-adaptive image enhancement method can maximum the contrast between the small target and the background of the two-dimensional SEM scanning images. Furthermore, the parameters are determined by the input data, not the users, which is self-adaptive and can reduce the error caused by human disturbance. It is an effective tool for the small target enhancement.

(2) For the testing image, the natural micro-cracks become more obvious to the naked eyes and the evaluation parameter increase from 2.15 to 8.67 after the modification. Also, the mean value from 153.47 to 87.10 and variance from 107.3 to 117.4 of the grayscale intensity histogram also show that after the modification, more information of the image can be employed for the following image processing.

(3) The multi-stage image segmentation method can combine the global information and local information to finish the segmentation process, which can classify the boundary pixels precisely. The three-dimensional fracture systems can be observed and the geometric parameters can be calculated. The comparison between the simulation results and experimental data shows that it can segment the thin fracture in the X-ray CT images with small error.

(4) For the testing three-dimensional model with hydraulic fracture systems, we can observe there are three fractures existing in the core and the fracture No. 1 serve as the flow channel of the fluids. The detailed parameters are as Table 3-3 shows. The simulated permeability from the segmentation results is 836.47 mD, with the minimum error of -22.1 % error comparing with the experimental data, about 1074.13 mD.

This study leads into several new ideas that can be followed as continuation of this work. Some of these potential future research studies are listed here:

(1) Most of the well-developed image processing algorithms are limited to one specific problem, which means that it is hard for any single image processing method to handle multi-target segmentation in one image. However, machine learning has shown great potential with the multi-target segmentation effectively, including k-means clustering, supported vector machine, and artificial neural network etc. How to apply the machine learning to precise multi-target segmentation would be the future work.

(2) The Kozeny-Carman relation used to calculate the permeability in this research belongs to the empirical formulas, which is not applicable to the natural micro-cracks with complex structures. So using molecular dynamics to simulate the fluid flow, especially in the nanoscale, would be another future work.

REFERENCES

1. Hoffman, B. T., & Shoaib, S. (2014). CO2 flooding to increase recovery for unconventional liquids-rich reservoirs. Journal of Energy Resources Technology, 136(2), 022801.
2. Jia, B., Tsau J., Barati, R. 2019. "A Review of the Current Progress of CO2 Injection EOR and Carbon Storage in Shale Oil Reservoirs". Fuel 236: 404-427.
3. Jia, B., Tsau, J., Barati, R. 2018. "Different Flow Behaviors of Low-pressure and High-pressure Carbon Dioxide in Shales". SPE Journal 23 (04): 1452-1468.
4. Todd, H. B., & Evans, J. G. (2016, May). Improved oil recovery IOR pilot projects in the Bakken formation. In SPE Low Perm Symposium. Society of Petroleum Engineers.
5. Jia, B., Tsau, J., Barati, R. 2018. "Experimental and Numerical Investigations of Permeability in Heterogeneous Fractured Tight Porous Media". Journal of Natural Gas Science and Engineering 58: 216-233.
6. Tahmasebi, P., Javadpour, F., & Sahimi, M. (2015). Multiscale and multiresolution modeling of shales and their flow and morphological properties. Scientific reports, 5, 16373.
7. Lai, J., Wang, G., Fan, Z., Chen, J., Qin, Z., Xiao, C., ... & Fan, X. (2017). Three-dimensional quantitative fracture analysis of tight gas sandstones using industrial computed tomography. Scientific Reports, 7(1), 1825.

8. Jia, B., Tsau, J.-S., & Barati, R. (2017, July 24). Different Flow Behaviors of Low-Pressure and High-Pressure CO2 in Shales. Unconventional Resources Technology Conference. doi:10.15530/URTEC-2017-2690239
9. Dewhurst, D. N., & Siggins, A. F. (2006). Impact of fabric, microcracks and stress field on shale anisotropy. Geophysical Journal International, 165(1), 135-148.
10. Xu, C., & Dowd, P. (2010). A new computer code for discrete fracture network modelling. Computers & Geosciences, 36(3), 292-301.
11. Jia, B., Tsau, J., Barati, R. 2018. "Measurement of CO2 Diffusion Coefficient in the Oil-saturated Porous Media". SPE-192703-MS. Presented at the Abu Dhabi International Petroleum Exhibition & Conference, Abu Dhabi, the United Arab Emirates, 12-15 Nov.
12. Otsu, N. (1979). A threshold selection method from gray-level histograms. IEEE transactions on systems, man, and cybernetics, 9(1), 62-66.
13. Christe, P., Turberg, P., Labiouse, V., Meuli, R., & Parriaux, A. (2011). An X-ray computed tomography-based index to characterize the quality of cataclastic carbonate rock samples. Engineering Geology, 117(3-4), 180-188.
14. Baker, D. R., Mancini, L., Polacci, M., Higgins, M. D., Gualda, G. A. R., Hill, R. J., & Rivers, M. L. (2012). An introduction to the application of X-ray microtomography to the three-dimensional study of igneous rocks. Lithos, 148, 262-276.
15. Wang, D. C., Vagnucci, A. H., & Li, C. C. (1983). Digital image enhancement: a survey. Computer Vision, Graphics, and Image Processing, 24(3), 363-381.
16. Cocklin, M. L., Gourlay, A. R., Jackson, P. H., Kaye, G., Kerr, I. H., & Lams, P. (1983). Digital processing of chest radiographs. Image and Vision Computing, 1(2), 67-78.

17. Pitas, I., & Nikolaidis, N. (2000). 3-D image processing algorithms. Wiley.
18. Lee, J. W., 2008, “Unconventional Resources,” ASME J. Energy Resour. Technol., 130(4), p. 040301.
19. Flannery, J., and Kraus, J., 2006, “Integrated Analysis of the Bakken Petroleum System, U.S. Williston Basin,” AAPG Annual Convention, Houston, Texas, April 10–12, AAPG Search and Discovery Article No. 10105.
20. Miller, B. A., Paneitz, J. M., Mullen, M. J., Meijs, R., Tunstall, K. M., & Garcia, M. (2008, January). The successful application of a compartmental completion technique used to isolate multiple hydraulic-fracture treatments in horizontal Bakken shale wells in North Dakota. In SPE Annual Technical Conference and Exhibition. Society of Petroleum Engineers.
21. Kumar, S., Hoffman, T., & Prasad, M. (2013, August). Upper and Lower Bakken Shale production contribution to the Middle Bakken reservoir. In Unconventional Resources Technology Conference (pp. 1-11). Society of Exploration Geophysicists, American Association of Petroleum Geologists, Society of Petroleum Engineers.
22. Dvorkin, J., Armbruster, M., Baldwin, C., Fang, Q., Derzhi, N., Gomez, C., ... & Nur, A. (2008). The future of rock physics: computational methods vs. lab testing. first break, 26(9).
23. Andrä, H., Combaret, N., Dvorkin, J., Glatt, E., Han, J., Kabel, M., ... & Marsh, M. (2013). Digital rock physics benchmarks—Part I: Imaging and segmentation. Computers & Geosciences, 50, 25-32.
24. Blunt, M. J., Jackson, M. D., Piri, M., & Valvatne, P. H. (2002). Detailed physics, predictive capabilities and macroscopic consequences for pore-network models of multiphase flow. Advances in Water Resources, 25(8-12), 1069-1089.

25. Bakke, S., & Øren, P. E. (1997). 3-D pore-scale modelling of sandstones and flow simulations in the pore networks. Spe Journal, 2(02), 136-149.
26. Lopez, O., Mock, A., Skretting, J., Petersen Jr, E. B., Øren, P. E., & Rustad, A. B. (2010). Investigation into the reliability of predictive pore-scale modeling for siliciclastic reservoir rocks. In SCA2010-41 presented at the 2010 SCA International Symposium, Halifax, Canada.
27. Wu, K., Jiang, Z., Couples, G. D., Van Dijke, M. I. J., & Sorbie, K. S. (2007, September). Reconstruction of multi-scale heterogeneous porous media and their flow prediction. In International Symposium of the Society of Core Analysts, Calgary, Canada.
28. Wu, K., Ryazanov, A., Van Dijke, M. I. J., Jiang, Z., Ma, J., Couples, G. D., & Sorbie, K. S. (2008). Validation of methods for multi-scale pore space reconstruction and their use in prediction of flow properties of carbonate. SCA Paper 2008-34.
29. Kalam, Z., Seraj, S., Bhatti, Z., Mock, A., Oren, P. E., Ravlo, V., & Lopez, O. (2012, August). Relative permeability assessment in a giant carbonate reservoir using Digital Rock Physics. In SCA2012-03, International Symposium, Aberdeen, United Kingdom.
30. Lopez, O., Mock, A., Øren, E. P., Long, H., Kalam, Z., Vahrenkamp, V., ... & Al Hosni, H. (2012, August). Validation of fundamental carbonate reservoir core properties using digital rock physics. In International Symposium of the Society of Core Analysts held in Aberdeen, Scotland, UK, SCA2012-19.
31. Hassler, G. L., & Brunner, E. (1945). Measurement of capillary pressures in small core samples. Transactions of the AIME, 160(01), 114-123.
32. Leverett, M. (1941). Capillary behavior in porous solids. Transactions of the AIME, 142(01), 152-169.

33. Purcell, W. R. (1949). Capillary pressures-their measurement using mercury and the calculation of permeability therefrom. Journal of Petroleum Technology, 1(2), 39-48.
34. Shikhov, I., & Arns, C. H. (2015). Evaluation of capillary pressure methods via digital rock simulations. Transport in Porous Media, 107(2), 623-640.
35. Dullien, F. A. (2012). Porous media: fluid transport and pore structure. Academic press.
36. Mavko, G., & Nur, A. (1997). The effect of a percolation threshold in the Kozeny-Carman relation. Geophysics, 62(5), 1480-1482.
37. Blair, S. C., Berge, P. A., & Berryman, J. G. (1993). Two-point correlation functions to characterize microgeometry and estimate permeabilities of synthetic and natural sandstones(No. UCRL-LR-114182). Lawrence Livermore National Lab., CA (United States).
38. Keehm, Y., Mukerji, T., & Nur, A. (2004). Permeability prediction from thin sections: 3D reconstruction and Lattice-Boltzmann flow simulation. Geophysical Research Letters, 31(4).
39. Tomutsa, L., Silin, D. B., & Radmilovic, V. (2007). Analysis of chalk petrophysical properties by means of submicron-scale pore imaging and modeling. SPE Reservoir Evaluation & Engineering, 10(03), 285-293.
40. Vogel, H. J., & Roth, K. (2001). Quantitative morphology and network representation of soil pore structure. Advances in water resources, 24(3-4), 233-242.
41. Orloff, J., Utlaut, M., Swanson, L., & Wagner, A. (2004). High resolution focused ion beams: FIB and its applications. Physics Today, 57(1), 54-55.
42. Kubis, A.J., Shiflet, G.J., Dunn, D.N., and Hill, R. 2004. Focused Ion Beam Tomography. Metallurgical and Material Transactions A 35A: 1935 – 1943. DOI: 10.1007/s11661-004-0142-4.

43. Lymberopoulos, D. P., & Payatakes, A. C. (1992). Derivation of topological, geometrical, and correlational properties of porous media from pore-chart analysis of serial section data. Journal of colloid and interface science, 150(1), 61-80.
44. Tomutsa, L., & Radmilovic, V. (2003). Focussed ion beam assisted three-dimensional rock imaging at submicron scale.
45. Tomutsa, L., & Silin, D. (2004). Nanoscale pore imaging and pore scale fluid flow modeling in chalk. [J]. SPE Reservoir Evaluation & Engineering, 2007, 10: 285 – 293.
46. Elliott J. T., Menedez B., Wong T.F. Imaging the pore structure of geomaterials [J]. Science, 1995, 268: 276 – 279.
47. Dunsmuir, John H., et al. "X-ray microtomography: a new tool for the characterization of porous media." SPE annual technical conference and exhibition. Society of Petroleum Engineers, 1991.
48. Dong H (2007) Micro-CT imaging and pore network extraction, PhD OR doctoral dissertation, Imperial College London, UK, p 213
49. Zhang T. MPS-Driven digital rock modeling and upscaling. Mathematical Geosciences. 2015 Nov 1;47(8):937-54.
50. Coenen, J., E. Tchouparova, and X. Jing. "Measurement parameters and resolution aspects of micro X-ray tomography for advanced core analysis." proceedings of International Symposium of the Society of Core Analysts. 2004.
51. Fredrich, J. T., Menendez, B., & Wong, T. F. (1995). Imaging the pore structure of geomaterials. Science, 268(5208), 276-279.

52. Curtis, M. E., Ambrose, R. J., & Sondergeld, C. H. (2010, January). Structural characterization of gas shales on the micro-and nano-scales. In Canadian unconventional resources and international petroleum conference. Society of Petroleum Engineers.
53. JOSHI, M. (1974). A class of stochastic models for porous media(probability distribution functions and random numbers)[Ph. D. Thesis].
54. Quiblier, J. A. (1984). A new three-dimensional modeling technique for studying porous media. Journal of Colloid and Interface Science, 98(1), 84-102.
55. Adler, P. M., Jacquin, C. G., & Quiblier, J. A. (1990). Flow in simulated porous media. International Journal of Multiphase Flow, 16(4), 691-712.
56. Ioannidis, M. A., Chatzis, I., & Kwiecien, M. J. (1999). Computer enhanced core analysis for petrophysical properties. Journal of Canadian Petroleum Technology, 38(03).
57. Hilfer, R. (1991). Geometric and dielectric characterization of porous media. Physical Review B, 44(1), 60.
58. Torquato, S., & Lu, B. (1993). Chord-length distribution function for two-phase random media. Physical Review E, 47(4), 2950.
59. Levitz, P. (1998). Off-lattice reconstruction of porous media: critical evaluation, geometrical confinement and molecular transport. Advances in Colloid and Interface Science, 76, 71-106.
60. Hazlett, R. D. (1997). Statistical characterization and stochastic modeling of pore networks in relation to fluid flow. Mathematical Geology, 29(6), 801-822.
61. Hidajat, I., Rastogi, A., Singh, M., & Mohanty, K. Transport properties of porous media from thin-sections (2001). In Paper SPE69623 presented 2001 at the SPE Latin American and Carribean Petroleum Engineering Conference, Buenos Aires, Argentina.

62. Bryant, S., & Blunt, M. (1992). Prediction of relative permeability in simple porous media. Physical Review A, 46(4), 2004.
63. Pilotti, M. (2000). Reconstruction of clastic porous media. Transport in Porous Media, 41(3), 359-364.
64. Coelho, D., Thovert, J. F., & Adler, P. M. (1997). Geometrical and transport properties of random packings of spheres and aspherical particles. Physical Review E, 55(2), 1959.
65. Okabe, H., & Blunt, M. J. (2005). Pore space reconstruction using multiple-point statistics. Journal of Petroleum Science and Engineering, 46(1-2), 121-137.
66. Wu, K., Nunan, N., Crawford, J. W., Young, I. M., & Ritz, K. (2004). An efficient Markov chain model for the simulation of heterogeneous soil structure. Soil Science Society of America Journal, 68(2), 346-351.
67. Ni, X., Chen, W., Li, Z., & Gao, X. (2017). Reconstruction of different scales of pore-fractures network of coal reservoir and its permeability prediction with Monte Carlo method. International Journal of Mining Science and Technology, 27(4), 693-699.
68. Hao, Q. (1987). On morphological character and origin of micropores in coal. Journal of China Coal Society, 4, 52-54.
69. Xue, G., Liu, H., & Li, W. (2012). Deformed coal types and pore characteristics in Hancheng coalmines in Eastern Weibei coalfields. International Journal of Mining Science and Technology, 22(5), 681-686.
70. Karimpouli, S., & Tahmasebi, P. (2016). Conditional reconstruction: An alternative strategy in digital rock physics. Geophysics, 81(4), D465-D477.

71. Tahmasebi, P., Hezarkhani, A., & Sahimi, M. (2012). Multiple-point geostatistical modeling based on the cross-correlation functions. Computational Geosciences, 16(3), 779-797.
72. Tahmasebi, P., Javadpour, F., & Sahimi, M. (2015). Three-dimensional stochastic characterization of shale SEM images. Transport in Porous Media, 110(3), 521-531.
73. Yeong, C. L. Y., & Torquato, S. (1998). Reconstructing random media. Physical Review E, 57(1), 495.
74. Manwart, C., Torquato, S., & Hilfer, R. (2000). Stochastic reconstruction of sandstones. Physical Review E, 62(1), 893.
75. Iacoviello, F., Backeberg, N., Brett, D. J. L., Gelb, J. and Shearing, P. R. Characterising Flow and Anisotropy in Gas Shale Rocks Using Mico- and Nano- X-Ray CT Imaging. 3rd International Conference on Tomography on Materials and Structures, Lund, Sweden, 26-30 June 2017.
76. Wildenschild, D., Vaz, C. M. P., Rivers, M. L., Rikard, D., & Christensen, B. S. B. (2002). Using X-ray computed tomography in hydrology: systems, resolutions, and limitations. Journal of Hydrology, 267(3-4), 285-297.
77. Wildenschild, D., & Sheppard, A. P. (2013). X-ray imaging and analysis techniques for quantifying pore-scale structure and processes in subsurface porous medium systems. Advances in Water Resources, 51, 217-246.
78. Ketcham, R. A., Slottke, D. T., & Sharp Jr, J. M. (2010). Three-dimensional measurement of fractures in heterogeneous materials using high-resolution X-ray computed tomography. Geosphere, 6(5), 499-514.

79. Porter, M. L., & Wildenschild, D. (2010). Image analysis algorithms for estimating porous media multiphase flow variables from computed microtomography data: a validation study. Computational Geosciences, 14(1), 15-30.
80. Elliot, T. R., & Heck, R. J. (2007). A comparison of 2D vs. 3D thresholding of X-ray CT imagery. Canadian Journal of Soil Science, 87(4), 405-412.
81. Noiriel, C., Gouze, P., & Madé, B. (2013). 3D analysis of geometry and flow changes in a limestone fracture during dissolution. Journal of hydrology, 486, 211-223.
82. Yushkevich, P. A., Piven, J., Cody, H., Ho, S., Gee, J. C., & Gerig, G. (2005, November). User-Guided Level Set Segmentation of Anatomical Structures with ITK-SNAP, Insight Jounral, Special Issue on ISC. NA-MIC/MICCAI workshop on open-source software.
83. Frangi, A. F., Niessen, W. J., Vincken, K. L., & Viergever, M. A. (1998, October). Multiscale vessel enhancement filtering. In International Conference on Medical Image Computing and Computer-Assisted Intervention (pp. 130-137). Springer, Berlin, Heidelberg.
84. Bogner, A., Jouneau, P. H., Thollet, G., Basset, D., & Gauthier, C. (2007). A history of scanning electron microscopy developments: towards “wet-STEM” imaging. Micron, 38(4), 390-401.
85. Fukunaga, K. (2013). Introduction to statistical pattern recognition. Elsevier.
86. Tubbs, J. D. (1987). A note on parametric image enhancement. Pattern Recognition, 20(6), 617-621.
87. Kirkpatrick, S., Gelatt, C. D., & Vecchi, M. P. (1983). Optimization by simulated annealing. science, 220(4598), 671-680.

88. Deutsch, C. V., & Journel, A. G. (1994). The application of simulated annealing to stochastic reservoir modeling. SPE Advanced Technology Series, 2(02), 222-227.
89. Metropolis, N., Rosenbluth, A. W., Rosenbluth, M. N., Teller, A. H., & Teller, E. (1953). Equation of state calculations by fast computing machines. The journal of chemical physics, 21(6), 1087-1092.
90. Wellington, S. L., & Vinegar, H. J. (1987). X-ray computerized tomography. Journal of Petroleum Technology, 39(08), 885-898.
91. Shannon, C. E. (1948). A mathematical theory of communication. Bell system technical journal, 27(3), 379-423.
92. Gonzalez, R. C. & Woods, R. E. (2002) Digital Image Processing, Prentice Hall, Upper Saddle River, New Jersy.
93. Journel, A. G., & Huijbregts, C. J. (1978). Mining geostatistics(Vol. 600). London: Academic press.
94. Antunes, I. M. H. R., & Albuquerque, M. T. D. (2013). Using indicator kriging for the evaluation of arsenic potential contamination in an abandoned mining area (Portugal). Science of the Total Environment, 442, 545-552.
95. Voorn, M., Exner, U., & Rath, A. (2013). Multiscale Hessian fracture filtering for the enhancement and segmentation of narrow fractures in 3D image data. Computers & geosciences, 57, 44-53.
96. Sato, Y., Nakajima, S., Atsumi, H., Koller, T., Gerig, G., Yoshida, S., Kikinis, R., 1997. 3D Multi-scale Line Filter for Segmentation and Visualization of Curvilinear Structures in Medical Images. In: Troccaz, J., Grimson, E., Mösges, R. (Eds.), Proceedings of First Joint

Conference, Computer Vision, Virtual Reality and Robotics in Medicine and Medical Robotics and Computer-Assisted Surgery, CMRMed-MRCAS, Grenoble, France, 1997. Lecture Notes in Computer Science 1205, pp. 213–222.

97. Lorenz, C., Carlsen, I.-C., Buzug, T.M., Fassnacht, C., Weese, J., 1997. Multi-scale Line Segmentation with Automatic Estimation of Width, Contrast and Tangential Direction in 2D and 3D Medical Images. In: Troccaz, J., Grimson, E., Mösges, R. (Eds.), Proceedings First Joint Conference, Computer Vision, Virtual Reality and Robotics in Medicine and Medical Robotics and Computer-Assisted Surgery, CMRMed-MRCAS, Grenoble, France, 1997. Lecture Notes in Computer Science 1205, pp. 233–242.
98. Darcy, H. (1856). Les fontaines publiques de la ville de Dijon. Paris: Dalmont
99. Sai, W., Kouqi, L., Kegang, L., & Hongsheng, W. (2018, August 21). Properties Evaluation of the Middle Bakken Formation Due to the CO2 Injection. American Rock Mechanics Association.